

# Spitzer's view on aromatic and aliphatic hydrocarbon emission in Herbig Ae stars

B. Acke<sup>1,2</sup>, J. Bouwman<sup>3</sup>, A. Juhász<sup>3</sup>, Th. Henning<sup>3</sup>, M.E. van den Ancker<sup>4</sup>, G. Meeus<sup>5</sup>,  
A.G.G.M. Tielens<sup>6</sup> and L.B.F.M. Waters<sup>1,7</sup>

bram@ster.kuleuven.be

## ABSTRACT

The chemistry of astronomical hydrocarbons, responsible for the well-known infrared emission features detected in a wide variety of targets, remains enigmatic. Here we focus on the group of young intermediate-mass Herbig Ae stars. We have analyzed the aliphatic and polycyclic aromatic hydrocarbon (PAH) emission features in the infrared spectra of a sample of 53 Herbig Ae stars, obtained with the Infrared Spectrograph aboard the Spitzer Space Telescope. We confirm that the PAH-to-stellar luminosity ratio is higher in targets with a flared dust disk. However, a few sources with a flattened dust disk still show relatively strong PAH emission. Since PAH molecules trace the gas disk, this indicates that gas disks may still be flared, while the dust disk has settled due to grain growth. There are indications that the strength of the 11.3- $\mu\text{m}$  feature also depends on dust disk structure, with flattened disks being less bright in this feature. We confirm that the CC bond features at 6.2 and 7.8  $\mu\text{m}$  shift to redder wavelengths with decreasing stellar effective temperature. Moreover, we show that this redshift is accompanied by a relative increase of aliphatic CH emission and a decrease of the aromatic 8.6- $\mu\text{m}$  CH feature strength. Cool stars in our sample are surrounded by hydrocarbons with a high aliphatic/aromatic CH ratio and a low aromatic CH/CC ratio, and vice versa for the hot stars. We conclude that, while the overall hydrocarbon emission strength depends on the dust disk's geometry, the relative differences seen in the IR emission features in disks around Herbig Ae stars are mainly due to chemical differences of the hydrocarbon molecules induced by the stellar UV field. Strong UV flux reduces the aliphatic component and emphasizes the spectral signature of the aromatic molecules in the IR spectra.

*Subject headings:* astrochemistry, stars: pre-main sequence, planetary systems: protoplanetary disks, infrared: general

---

<sup>1</sup>Instituut voor Sterrenkunde, K.U.Leuven, Celestijnenlaan 200D, B-3001 Leuven, Belgium

<sup>2</sup>Postdoctoral Fellow of the Fund for Scientific Research, Flanders.

<sup>3</sup>Max-Planck-Institute for Astronomy, Königstuhl 17, D-69117 Heidelberg, Germany

<sup>4</sup>European Southern Observatory, Karl-Schwarzschild-Strasse 2, D-85748 Garching bei München, Germany

<sup>5</sup>Universidad Autónoma de Madrid, Departamento de Física Teórica C-XV, 28049 Madrid, Spain

<sup>6</sup>Leiden Observatory, P.O. Box 9513, NL-2300 RA Leiden, the Netherlands

<sup>7</sup>Astronomical Institute "Anton Pannekoek", University of Amsterdam, Science Park 904, 1098 XH Amsterdam, the

## 1. Introduction

Herbig Ae stars are pre- and zero-age main-sequence stars of a few solar masses. They are surrounded by a circumstellar disk, a remnant of the star-formation process. Meeus et al. (2001) have classified the spectral energy distributions (SEDs) of these targets into two groups, which reflect the geometry of the dust disk. Group I sources have a strongly flared outer disk, while the disks in group II sources are flatter.

---

Netherlands

The outer disk surface of the latter lies in the shadow of the inner disk (Dullemond et al. 2001; Dullemond & Dominik 2004a; Acke et al. 2009). Both theory (Dullemond & Dominik 2004b; Meijer et al. 2008) and observations (Acke et al. 2004) indicate that this difference in disk geometry is due to dust grain growth and subsequent settling to the mid-plane. Also the smallest dust grains in the disk surface layer appear to show evidence for sedimentation, although the correlation between grain size and flaring could also be due to a radial gradient in grain size (Bouwman et al. 2008; Furlan et al. 2009, Juhász et al. 2010).

The material content of these circumstellar disks has been primarily studied based on infrared (IR) spectra obtained with ground-based instruments and spectrographs aboard satellite missions such as the Infrared Space Observatory (ISO, Kessler et al. 1996) and, more recently, the Spitzer Space Telescope (Werner et al. 2004a). IR spectroscopy probes the thermal emission of the warm surface layer of the disk. Micrometer-sized silicate dust grains, both amorphous and crystalline, are commonly detected both because of their abundance and the fact that their optical properties give rise to strong bands in this wavelength regime (see the review by Henning & Meeus 2009). The spectral fingerprint of the silicates has been interpreted in terms of grain growth and crystallisation of the smallest grains in the disk (e.g., Bouwman et al. 2001; Acke & van den Ancker 2004; van Boekel et al. 2005; Sargent et al. 2009). Besides silicate bands, the IR spectra of many Herbig Ae stars display strong emission features from polycyclic aromatic hydrocarbon (PAH) molecules. In this paper, we focus on these molecules. They trace the carbonaceous component of the circumstellar matter.

Next to its detection in Herbig Ae stars, PAH emission is observed in a multitude of objects and environments, including the interstellar medium (ISM), T Tauri stars, reflection nebulae (RNe), and, occasionally, evolved stars. The emission features are the result of IR fluorescence of PAH molecules pumped by ultraviolet radiation. Ionized PAHs can also be excited by optical and near-IR photons (e.g., Li & Draine 2002; Mattioda et al. 2005a,b). Because of the stochastic nature of the heating process, PAH emission can be seen even far from the illuminating UV

source. For a comprehensive review on interstellar PAHs, we refer to Tielens (2008).

Astronomical PAH features come in different flavors and show a broad variety in shape, wavelength position and relative intensity. It is believed that this diversity has its origin in a different chemical constitution and ionization state of the carriers. The wealth of laboratory measurements and theoretical computations of hydrocarbon IR spectra has deepened our understanding of the emission features. While the features at  $3.3\ \mu\text{m}$ ,  $8.6\ \mu\text{m}$  and in the  $10\text{--}14\text{-}\mu\text{m}$  range are attributed to CH stretching and bending modes, the features at  $6.2\ \mu\text{m}$  and  $7\text{--}9\ \mu\text{m}$  are due to CC stretching modes (Allamandola et al. 1989). Ionization enhances the strength of the CC modes ( $6\text{--}9\ \mu\text{m}$ ) relative to the CH modes ( $10\text{--}14\ \mu\text{m}$ ). The molecular size mainly affects the CC features, while the changes in the CH modes are expected to be more subtle. The  $8.6\text{-}\mu\text{m}$  feature, attributed to the CH in-plane bending mode, is suggested to be produced by large ( $N_C \sim 100$ ) compact PAHs only (Bauschlicher et al. 2008). The  $7\text{--}9\text{-}\mu\text{m}$  complex consists of several sub-bands, with the most prominent at  $7.6$  and  $7.8\ \mu\text{m}$  produced by small and large ionized PAHs respectively (Bauschlicher et al. 2008, 2009).

Despite our theoretical and experimental knowledge of PAHs, none of the astronomical spectra can be satisfactorily fitted with the available set of computed/laboratory spectra. Many analyses therefore focus on observational correlations. Features produced by CC modes correlate better with each other than with CH-mode features, and vice versa. Hony et al. (2001) have investigated the CH out-of-plane modes ( $10\text{--}14\ \mu\text{m}$ ) in a sample of various astronomical targets. The  $11.3\text{-}\mu\text{m}$  feature is ascribed to lone (solo) CH groups found in PAH molecules with long straight edges, while the features at  $12.0$ ,  $12.7$ ,  $13.5$  and  $14.2\ \mu\text{m}$  are linked to duo, trio, quartet and quintet CH modes, indicative of corners in the molecular structure.

Peeters et al. (2002) categorized the astronomical PAH spectra in 3 classes, reflecting the peak position of the major features in the  $6\text{--}9\text{-}\mu\text{m}$  range. Class A contains the targets with the bluest features, mainly general ISM sources, HII regions and RNe. Class C, characterized by the reddest features, consists mainly of cool carbon-rich (post-)AGB and red giant stars (Sloan et al. 2007;

Gielen et al. 2009; Smolders et al. 2010); Class B sources have intermediate feature peak positions, and include the Herbig Ae stars and most PNe. Sloan et al. (2005) and Sloan (2008) propose to categorize the PAH spectra of Herbig Ae stars in a new class (dubbed Class B'). Their 7–9- $\mu\text{m}$  features show an extended red wing beyond 8.0  $\mu\text{m}$ , which is absent in the Class B features of PNe.

The wavelength shift of the features has been observationally linked to the effective temperature of the central star (Sloan et al. 2007; Boersma et al. 2008; Keller et al. 2008), with cooler stars displaying redshifted IR emission features. This indicates that the chemistry of the emitting hydrocarbon molecules depends on the properties of the stellar radiation field.

A plateau with superimposed narrow features has been detected in the 15–21- $\mu\text{m}$  range in a number of targets (Beintema et al. 1996; Van Kerckhoven et al. 2000; Sturm et al. 2000; Werner et al. 2004b; Sellgren et al. 2007). It is our observation that most of these targets, if not all, belong to Class A. Peeters et al. (2004) attribute the narrow features to out-of-plane skeletal CCC modes of gas-phase PAH molecules. The authors argue that the latter are large elongated PAHs with straight edges and few pendant rings.

All features mentioned above are ascribed to PAHs. Their fundamental constituents are aromatic (i.e. benzenoid) rings. Aliphatic hydrocarbon molecules do not have such rings. The features at 6.8 and 7.2  $\mu\text{m}$ , detected in a number of sources, are attributed to aliphatic bonds (e.g., Furton et al. 1999; Chiar et al. 2000; Dartois et al. 2007; however, see also Bauschlicher et al. 2009). The 6.8- $\mu\text{m}$  feature is linked to CH bending modes in both  $\text{CH}_2$  and  $\text{CH}_3$  functional groups, the 7.2- $\mu\text{m}$  feature only to  $\text{CH}_3$ . Hydrocarbon molecules with mixed hybridization display aromatic as well as aliphatic emission features.

The work presented in this paper is performed in the framework of an infrared study of a large sample of Herbig Ae stars, based on IR spectra collected with the Spitzer Space Telescope. Acke et al. (2009) investigated the geometry of the dust disk based on the strength and slope of the thermal infrared emission. We refine the interpretation of the Meeus group I/group II classification and show that the height of the inner disk varies over the sample. This leads to a varying amount

of shadowing of the outer disk and a change in the shape of the infrared continuum emission. Juhász et al. (2010, submitted to ApJ; hereafter J10) present the full spectral decomposition into dust and continuum components. The characteristics of the amorphous and crystalline silicate content of the upper disk layers are related to stellar and disk properties. The current paper focuses on the IR emission features produced by aromatic and aliphatic hydrocarbon molecules. Given their importance in the surface layers of circumstellar disks, where they increase the gas temperature through photoelectric heating and provide the surface for chemical reactions, a better characterization of their chemical properties is needed to improve our understanding of circumstellar disk structure and evolution. Furthermore, the life cycle of hydrocarbon molecules in space is poorly understood (e.g., Henning & Salama 1998). Here, we aim to contribute to these topics.

## 2. Data set

### 2.1. Spitzer IRS spectra

We have gathered infrared spectra of 53 isolated Herbig Ae stars obtained with the Infrared Spectrograph (IRS, Houck et al. 2004) aboard the Spitzer Space Telescope. Most of these sources were observed within the programs *The mineralogy of proto-planetary disks surrounding Herbig Ae/Be stars* (PID 3470, PI J. Bouwman) and *Probing the disk mineralogy and geometry of Herbig Ae/Be stars* (PID 20308, PI B. Acke). The spectra are characterized by a very high signal-to-noise ratio, typically several hundreds. For a detailed description of the data reduction process, the reduced spectra, and the sample targets, we refer to J10.

For each of the sample targets, published photometric data are gathered to compile the spectral energy distributions. A reddened Kurucz (1991) model was fitted to the observed UV-optical photometry. The circumstellar IR excess flux is characterized by several parameters such as excess magnitudes and spectral indices in the near-to-far-IR and at (sub-)mm wavelengths. Table 1 summarizes a few of these parameters. Based on the SED, we have classified the sample into the Meeus groups according to the method proposed by van Boekel et al. (2005). For details, we refer

to J10.

## 2.2. Extraction of the PAH spectrum

In this section, we describe how the hydrocarbon emission features are separated from the thermal emission of the circumstellar dust. The IRS spectrum was split into two wavelength intervals (5–7 and 7–14  $\mu\text{m}$ ) which are treated differently.

The 5–7- $\mu\text{m}$  wavelength range is characterized by the presence of carbonaceous features on top of a relatively smooth dust continuum. In this interval, the continuum was approximated with a single spline through anchor points at 5.35, 5.45, 5.58, 5.82, 6.66, 7.06, 7.37, 7.40, 7.55 and 7.70  $\mu\text{m}$ . Note that the broad 7–9- $\mu\text{m}$  PAH feature is treated as a continuum to the weaker features that are located on top of it. The features in the continuum-subtracted spectrum are measured according to the procedure described in Sect. 2.3.

The PAH features in the 7–14- $\mu\text{m}$  wavelength range are less easily extracted from the original spectrum, as the underlying “continuum” may contain strong features of amorphous and crystalline silicate dust. Keller et al. (2008) show that spline fits are only applicable to spectra with a high feature-to-continuum contrast. In spectra with strong silicate bands, artificial features are created. Keller et al. (2008) therefore only consider the strongest PAH sources in their analysis. In an attempt to reach weak PAH features, we follow a different approach. Six of our sample targets have a spectrum characterized by strong PAH emission and by the absence/weakness of silicate features. These sources are HD 34282, RR Tau, HD 97048, HD 135344B, HD 141569 and HD 169142. Their PAH profiles are representative for those observed in the entire sample, covering the observed range in feature peak position, shape and width. A single spline was fitted through continuum anchor points at 5.52, 5.83, 6.66, 7.06, 9.54, 10.32, 13.08 and 13.85  $\mu\text{m}$ . The spline-subtracted spectra were used as PAH template spectra. Each template spectrum is cut into five separate “PAH feature complexes” at 5.5–7.0, 7.0–8.2, 8.2–9.2, 10.5–12.3 and 12.2–13.5  $\mu\text{m}$ . The procedure to obtain full 5–16- $\mu\text{m}$  spectral decomposition of the IRS spectra makes use of these templates. For each of the PAH complexes, the fitting routine picks one of the six template spectra, appropriately rescaled. The best fit for a certain

target includes a PAH spectrum which is a scaled combination of five template spectra. The inclusion of PAH template spectra prevents the fitting routine from compensating for the PAH features using the dust species in the model. Hence, the results of the dust fit should be more reliable. Moreover, after subtraction of the dust+continuum part of the best spectral fit to the original spectrum, the residual spectrum is the real PAH spectrum of the target. Fig. 1 shows the residual spectra. A detailed description of the dust modeling can be found in J10.

The procedure works well for most spectra. However, some residuals of the crystalline silicate features remain. This is due to a slight mismatch in peak wavelength between the observations and the computed silicate opacities (see J10 for details). The residuals hamper an accurate extraction of the PAH features with low peak-to-continuum ratios, especially in the 10–14- $\mu\text{m}$  region. Fig. 2 shows the resulting PAH spectra of two silicate-dominated targets. In the case of HD 35187, the procedure leads to an excellent result; for HD 244604, the extraction method creates strong artifacts in the 7–12- $\mu\text{m}$  region. The features in this region cannot be detected with 3-sigma significance.

The aromatic-CCC bending-mode feature is present in the 16–19- $\mu\text{m}$  range of a handful of sources. A spline through anchor points at 14.0, 14.8, 15.0, 15.4, 15.6, 18.1, 18.6, 19.3 and 19.5  $\mu\text{m}$ , approximating the underlying continuum, is subtracted.

## 2.3. Derivation of the observables

We aim at investigating whether the aliphatic and aromatic features observed in the spectra display the signature of chemical diversity and evolution of their carriers. To do so, the detected features are captured in a number of representative parameters. We stay as close as possible to the real measurements, and avoid the use of approximate line profiles such as Gaussian curves. In this section, we describe how the observables are obtained.

For each feature, a wavelength interval indicating its blue and red limits is defined based on the best-quality PAH-dominated spectra where the feature is detected (HD 34282, HD 97048,

HD 169142 and RR Tau). This wavelength interval was visually checked for each individual target in order to avoid false detections. To minimize the effect of residuals of the continuum subtraction, either the spline or dust model, a straight line which connects the blue and red limit is subtracted from the spectrum. The integrated line flux is the total integral of the resulting continuum-subtracted feature. Furthermore, the centroid position of the feature (i.e. the flux-weighted barycenter), the full width at half maximum (FWHM), the peak position and the peak flux are determined. Uncertainties on the first two parameters were deduced directly from the error bars on the spectrum. For the FWHM, peak position and peak flux, the following approach was taken: 100 spectra of the feature were simulated around the original spectrum, assuming a Gaussian error distribution with a sigma equal to the error in each spectral pixel. In each of these spectra, we determine the FWHM, peak position and peak flux of the feature. The standard deviation of these measurements is taken as the error on the feature parameter determined from the original spectrum.

To quantify the influence of our choice of the feature wavelength limits on the measurements, the procedure described above was repeated over a slightly larger wavelength interval: the blue limit was shifted one spectral pixel to the blue, and the red limit one pixel to the red. The difference between the two values for each parameter was used to estimate the error induced by the choice of wavelength limits. The final error on our measurements is the square root of the quadratic sum of the latter, systematic, error and the observational error described above.

Some of the features are a blend of individual features. When the spectral resolution allows it, the components of these complexes are separated. The largest feature is considered to be part of the underlying continuum of the smaller feature(s). In general, a spline is fitted to the wing of the large feature on one side of the smaller feature, and to the continuum (which is zero in the continuum-subtracted spectra) on the other side. The residual spectrum is that of the smaller feature, the larger feature is set equal to the spline in the region where the small feature is located. The parameters of both features are determined as described above. Fig. 3 shows the procedure for the 6- $\mu\text{m}$

region. This method was also used to separate the 7-<sup>9</sup> and 8.6- $\mu\text{m}$  features and the 10.6, 11.3, 12.0 and 12.7- $\mu\text{m}$  features (Fig. 4). Again, an a priori fixed set of anchor points was used for all stars in the sample.

From the line fluxes of the detected aromatic features, i.e. all features except those at 6.8 and 7.2  $\mu\text{m}$ , a total PAH flux is computed. The same is done for the aliphatic features. The ratio of the aliphatic and aromatic line fluxes is equal to their luminosity ratio  $L_{\text{ali}}/L_{\text{PAH}}$ . We also compute the feature-to-stellar luminosity ratio  $L_f/L_*$  for each feature  $f$  separately. The stellar luminosity is that of the Kurucz model fitted to the SED.

### 3. Analysis

#### 3.1. Detected features

A detected feature is defined as a feature with a continuum-subtracted peak flux exceeding the 3-sigma level. Strong aromatic features are detected at the well-known wavelengths 6.2, 7.8, 8.6, 11.3 and 12.7  $\mu\text{m}$ . Secondary features are observed at 5.7, 6.0, 10.6, 12.0 and 13.5  $\mu\text{m}$ . We did not detect the feature at 14.3  $\mu\text{m}$ , linked to the quintet CH out-of-plane bending mode, in any of the sample sources. The 16–19- $\mu\text{m}$  complex is measured in five targets (see Fig. 5). Aliphatic features are detected in a number of sources, at 6.8 and 7.2  $\mu\text{m}$ . In total, 13 spectrally separated features are identified.

In 37 of the 53 sample sources (70%), one or more significant PAH features have been detected. The detection rate is 16/20 (80%) in group I, and 21/33 (64%) in group II. Aliphatic features are found in 22 of the 40 sources for which a short-wavelength spectrum is available (55%). The aliphatic detection rate is 11/15 in group I (73%) and 11/25 in group II (44%).

Table 2 gives an overview of the sample-average parameters of the detected features. We indicate the possible carriers of each of the features as mentioned in the literature. Tables 3 and 4 list the measured line fluxes and upper limits. Table 5 gives the fractional feature-to-stellar luminosities and PAH-to-aliphatic luminosities.

<sup>1</sup>Because almost all our sample targets belong to Class B', with the dominant sub-band at 7.8  $\mu\text{m}$ , we hereafter refer to this feature as the 7.8- $\mu\text{m}$  feature.

### 3.2. Correlations

We searched for correlations between the feature parameters, the stellar parameters and the disk parameters derived from the SED. To compare two parameters, the Kendall tau-rank correlation coefficient was computed, which is a non-parametric statistic (Kendall 1938). A correlation is marked statistically significant if its p-value is less than 1%, under the assumption that no correlation is present, before *and* after removal of the outliers. Hence, apparent correlations based on only a few data points are removed, as well as those induced by outliers.

The sample targets are classified in the two Meeus groups. In all figures presented in this paper, group I sources are the black dots, group II the red dots. For all feature parameters, we checked whether their values are significantly different in one group with respect to the other. We used the non-parametric Wilcoxon rank-sum test for assessing whether two independent samples of observations come from the same distribution (Mann & Whitney 1947).

## 4. Results

### 4.1. The chemical diversity of PAHs in Herbig Ae stars

The Peeters spectral classification is interpreted in terms of chemical diversity of the hydrocarbon carriers of the features. The CC stretching feature at  $6.2\ \mu\text{m}$  in astronomical spectra is shifted with respect to its theoretical position at  $6.4\ \mu\text{m}$ . This is also the case in our sample. The shift has been ascribed to the inclusion of nitrogen atoms in the PAH skeletal structure. The feature is increasingly bluer when the N atom is substituted deeper in the PAH molecule (Hudgins et al. 2005). Also the anion-to-cation ratio may play a role (Bauschlicher et al. 2009). However, the peak positions of the  $6.2$  and  $7.8\text{-}\mu\text{m}$  features correlate (Fig. 6). While the general blueshift of the feature from  $6.4$  to  $6.2\ \mu\text{m}$  may still be attributed to nitrogen pollution, the latter cannot account for the progressive shift of the  $6.2$  and  $7.8\text{-}\mu\text{m}$  features. Pino et al. (2008) have performed laboratory measurements and show that a shift of the  $6.2\text{-}\mu\text{m}$  feature to longer wavelengths points to a higher aliphatic/aromatic content of the hydrocar-

bon mixture.

The feature-to-stellar luminosity ratios of almost all PAH features (at  $5.7$ ,  $6.0$ ,  $6.2$ ,  $7.8$ ,  $8.6$ ,  $10.6$ ,  $11.3$ ,  $12.0$  and  $12.7\ \mu\text{m}$ ) correlate with each other. This indicates that these PAH features appear together in the spectrum of a Herbig Ae star, and roughly scale together in strength. The relative strengths of the aliphatic and aromatic features, on the other hand, are not connected. We also find dozens of significant correlations of line flux ratios. The strongest correlation in our sample is between the  $6.2$  and  $7.8\text{-}\mu\text{m}$  features, both linked to CC modes. Tight connections were also found between the  $6.2$  and  $8.6\text{-}\mu\text{m}$ , the  $7.8$  and  $8.6\text{-}\mu\text{m}$ , and the  $11.3$  and  $12.7\text{-}\mu\text{m}$  features. Fig. 7 shows two examples of such correlations. The  $6.2$ ,  $7.8$  and  $8.6\text{-}\mu\text{m}$  features, attributed to ionized PAHs, are closely related to each other, as well as the features in the  $11\text{--}14\text{-}\mu\text{m}$  range, due to out-of-plane CH bending modes of neutral and ionized PAHs.

Hony et al. (2001) and Keller et al. (2008) discuss the link between the  $6.2/11.3$  and  $12.7/11.3$  line flux ratios. The first is interpreted as a measure for the degree of ionization, the second as a measure for the irregularity of the PAH's edge. The authors conclude that both ratios point to the degree of processing of the molecules. An increase in PAH molecular size also enhances the  $11.3\text{-}\mu\text{m}$  feature with respect to the  $6.2$  and  $12.7\text{-}\mu\text{m}$  features. We confirm this correlation between line flux ratios (p-value 1%). Keller et al. (2008) also find a decrease of the  $12.7/11.3$  ratio with decreasing stellar temperature. Our data do not show a clear correlation for the entire sample, but a correlation may be present for the group I sources only (Fig. 8). In any case, it appears that the  $12.7/11.3$  ratio is different in group I and II. We come back to this issue in the Sect. 4.4.

### 4.2. The $16\text{--}19\text{-}\mu\text{m}$ feature

Five stars (HD 34282, HD 36917, HD 97048, HD 100453 and HD 135344B) display an emission feature at  $16\text{--}19\ \mu\text{m}$ . The complex is attributed to the out-of-plane skeletal modes of large elongated PAH molecules (Peeters et al. 2004). The detection is remarkable because our sample targets are Class B' sources, while this feature complex is mostly seen in ISM-like Class A objects.

The strength and shape of the 16–19- $\mu\text{m}$  feature is not correlated to those of other features at shorter wavelengths. This is consistent with the interpretation that the short- and long-wavelength features are produced by different PAH populations. Four of the five targets with detected 16–19- $\mu\text{m}$  emission have a very red SED: their 30/13.5 continuum flux ratios are among the highest in the sample (see Table 1). Possibly, these sources are still surrounded by an envelope or extended outer disk in which the chemistry of the PAH molecules is governed by the tenuous but harsh interstellar UV field rather than that of the central star (see also Boersma et al. 2008).

Alternatively, the detection or otherwise of the feature may be due to a contrast effect. The continuum emission at 20  $\mu\text{m}$  is dominated by warm dust grains close to the central star, while the feature is produced in the outer disk via stochastic heating. The extreme 30/13.5 continuum flux ratio could indicate that, while the outer disk is still strongly flared, the inner disk has started to settle. An additional indication for this hypothesis could be the absence of the 10- $\mu\text{m}$  silicate emission feature in HD 34282, HD 97048, HD 100453 and HD 135344B<sup>2</sup>: when silicate dust coagulates and grows beyond several  $\mu\text{ms}$ , the emission bands in the mid-IR range disappear. The settling of the inner disk implies a reduction of the warm continuum emission at 20  $\mu\text{m}$  and hence an increased feature-to-continuum contrast. Later on, when the outer disk eventually starts to settle as well, the strength of the 16–19- $\mu\text{m}$  complex decreases together with the degree of flaring.

### 4.3. Hydrocarbon molecules and silicate grains

Based on the IR spectra, the properties of the (sub-) $\mu\text{m}$ -sized silicate grains in the upper layers of the disk can be derived. J10 show that only a few dust species contribute to the emission-band spectrum: amorphous silicates with olivine and pyroxene stoichiometry, the Mg-rich crystalline silicates forsterite and enstatite, and silica. Different grain sizes (0.1, 2 and 5  $\mu\text{m}$ ) are included in the

spectral fit. The fitting routine was performed on two wavelength ranges, 5–17  $\mu\text{m}$  and 17–35  $\mu\text{m}$ , to sample the hot dust close to the star and the cooler dust further out and deeper in the disk. This yielded the mass fraction of each of the species, for each grain size and in both intervals. For details, we refer to J10.

We have taken the dust mass fractions and searched for correlations with the hydrocarbon feature parameters derived here. None were found with a p-value below 5%, with one marked exception. The FWHM of the 6.2- $\mu\text{m}$  feature appears to be strongly correlated to the mass fraction of the 0.1- $\mu\text{m}$  silica grains, derived from the spectral fit to the 17–35  $\mu\text{m}$  spectrum (Fig. 9). Targets with a broad 6.2- $\mu\text{m}$  feature have less small silica grains in the cold/outer disk. It is conceivable that this is a statistical false-positive correlation out of the  $\sim 3000$  investigated comparisons between silicate and PAH parameters. However, the correlation has a very low p-value ( $1 \times 10^{-5}$ ). The probability that such a strong random correlation would occur here is only 3%. Also the fact that both parameters were measured in disjunct wavelength ranges in the spectrum, strengthens our confidence in the reality of the correlation.

The relation is unexpected and we can only speculate about its origin. PAHs are stochastically heated and their emission comes from further out in the disk surface, where grains in thermal equilibrium are much colder. It is likely that the PAHs producing the 6.2- $\mu\text{m}$  feature and the cold silica grains are located in the same physical region. (Hudgins et al. 2005) mention that peripheral oxygen groups can influence the 6.2- $\mu\text{m}$  feature position. Perhaps the cumulative effect of a population of PAH molecules with such peripheral groups broadens the 6.2- $\mu\text{m}$  feature. The observed correlation would then indicate that the 0.1- $\mu\text{m}$  silica grains and the PAH molecules are chemically competing for oxygen atoms: the oxygen is either locked in peripheral groups of PAH molecules, or included in 0.1- $\mu\text{m}$  silica grains.

### 4.4. Influence of the disk geometry

We checked for differences between Meeus group I and II sources. This classification is based on the thermal infrared emission seen in the SED, and thus indicates the geometry of the *dust* disk. Group I sources have a flared dust disk, while the

<sup>2</sup> On the other hand, HD 37411, RR Tau, HD 141569 and HD 169142 are also PAH sources without a 10- $\mu\text{m}$  silicate feature, but their spectra do not show the 16–19- $\mu\text{m}$  feature.

dust disk in the group II members has flattened, probably as a result of dust grain growth and sedimentation to the midplane.

In a number of papers (Meeus et al. 2001; Acke & van den Ancker 2004; Habart et al. 2004), it has been claimed that the strength of the PAH features depends on the disk geometry. A flared disk has a larger illuminated surface. Group I sources are therefore expected to produce stronger PAH emission. However, Keller et al. (2008) do not find this correlation in their sample of Herbig Ae/Be stars. Here, we elaborate on this.

Making use of radiative transfer models, Meijer et al. (2008) demonstrate that the degree of flaring of the dust disk largely depends on one parameter: the mass in sub- $\mu\text{m}$ -sized dust grains. A higher dust mass results in a higher opacity at optical wavelengths, a warmer outer disk, and more flaring. Acke et al. (2009) show in their Fig. 3 that the flux excess above the stellar photosphere at  $60\ \mu\text{m}$  is a tracer for the dust mass, and hence for the degree of flaring. Fig. 10 compares the IRAS  $60\text{-}\mu\text{m}$  excess to the excess at  $30\ \mu\text{m}$ . The latter is determined from the Spitzer IRS spectra and the Kurucz model for the star<sup>3</sup>. A very strong correlation is noted, which indicates that also the excess at  $30\ \mu\text{m}$  traces the disk geometry. Because IRAS  $60\text{-}\mu\text{m}$  photometry is not available for all sample sources, and to rely only on the Spitzer IRS spectra, we use the excess at  $30\ \mu\text{m}$  in the following.

We investigate whether the luminosity of individual PAH features, relative to the stellar luminosity, correlates with the excess at  $30\ \mu\text{m}$ . The former is the fraction of stellar flux captured and re-emitted by the PAH molecules. We find that the feature-to-stellar luminosity of most of the features ( $5.7$ ,  $6.0$ ,  $6.2$ ,  $7.8$ ,  $8.6$ ,  $10.6$ , and  $12.7\ \mu\text{m}$ ) increases significantly with increasing  $30\text{-}\mu\text{m}$  excess. Fig. 11 shows the correlation for the most frequently detected feature, at  $6.2\ \mu\text{m}$ . Also the total PAH-to-stellar luminosity ratio correlates with the far-IR excess (p-value  $9 \times 10^{-5}$ ).

It is clear that the disk geometry influences the PAH-to-stellar luminosity ratio. However, the large amount of scatter indicates that the degree of flaring is not the only parameter. Source-to-source differences in PAH abundance are certainly

important. Furthermore, there are targets which have a flattened dust disk (group II), but are still strong PAH emitters. A solution to this apparent discrepancy has been proposed in a few recent papers. van der Plas et al. (2008) and Fedele et al. (2008) show that the dust disk can decouple from the gas disk, probably due to dust grain growth and subsequent settling to the midplane. This results in a flattened dust disk, while the gas disk can still have a flared structure. Verhoeff et al. (2010) have further elaborated on this idea and performed detailed modeling of HD 95881, a target with an extremely blue group II-type SED, but strong PAH emission.

Along the same lines, Dullemond et al. (2007) have modeled dust sedimentation in protoplanetary disks with PAHs. They find that, if the PAH abundance stays the same, sources with sedimented dust disks should display *more* pronounced PAH features than disks with perfect vertical mixing. Two effects are important: the reduction of the continuum emission (increased contrast) and the increased amount of UV-exposed PAH molecules (increased PAH luminosity). Under the assumptions of the models, a decrease in far-IR continuum emission should be accompanied by an increase of PAH luminosity. The opposite trend is observed, however. Dullemond et al. (2007) speculate that a significant fraction of the PAHs is removed through aggregation. In any case, a reduction of PAH abundance in the flared gas disk above the dust disk, e.g. through PAH photodestruction, is necessary to reconcile theory and observations.

We found indications that there is indeed a small difference in PAH chemistry between flared and flattened disks. There is a strong correlation between the peak flux ratios  $11.3/6.2$  and  $11.3/7.8$  (Fig. 12). This is not surprising, as the  $6.2$  and  $7.8\text{-}\mu\text{m}$  features are both CC modes and thus strongly linked to each other (see Sect. 4.1). From the figure, however, it seems that the distributions of the  $11.3/6.2$  and the  $11.3/7.8$  ratios are shifted towards lower values in group II. Also the  $12.7/11.3$  line flux ratio appears to be higher in this group ( $0.29 \pm 0.08$  vs.  $0.22 \pm 0.05$  in group I, p-value 0.5%). This suggests that the  $11.3\text{-}\mu\text{m}$  feature is weak in the targets with a small far-IR excess, and may indicate that the PAH molecules in targets with a flattened dust disk are more processed, i.e.

<sup>3</sup>The excess magnitude is defined as  $M = 2.5 \log F_{\text{tot}}/F_{\star}$ .



rough-edged and/or smaller, than those in flared disks.

#### 4.5. Aliphatic versus aromatic hydrocarbons

Almost all stars in our sample display Class B' PAH features, but it is clear that even within this class, spectral differences occur. Here we argue that these changes are mainly due to the stellar UV field to which the hydrocarbon molecules are exposed.

The centroid (and peak) position of the 7.8- $\mu\text{m}$  feature decreases with increasing effective temperature. Fig. 13 shows the data for our sample of Herbig Ae stars. We have expanded the sample with a set of pre-main-sequence stars of different stellar masses, obtained in other Spitzer IRS programs. On the low-mass end, we have included five T Tauri stars with detected PAH emission. RX J1842.9–3532, RX J1852.3–3700, HD 143006, RX J1612.6–1859A and 1RXS J132207.2–693812 were observed within the *Formation and Evolution of Planetary Systems* (FEPS) Legacy Science Program (PID 148, PI M. Meyer). The spectra and stellar effective temperatures were taken from Bouwman et al. (2008). On the high-mass end, six Herbig Be stars were added. The spectra of HD 290770, Hen 3–180, LkH $\alpha$  257, PDS 216, PDS 344 and RNO 6 were acquired within the Spitzer Program *Structure and composition of disks surrounding Herbig Be stars* (PID 50180, PI M. van den Ancker). Their effective temperature has been estimated based on their spectral type. The correlation between 7.8- $\mu\text{m}$  centroid position and  $T_{\text{eff}}$  is clear for the Herbig Ae stars, and is even more prominent when including the lower- and higher-mass young stars. The contribution of the red sub-bands appears to be more significant in cooler stars than in hotter stars, which is supported by the fact that the width of the 7.8- $\mu\text{m}$  feature increases with redshift (Fig. 14). Finally, also the peak and centroid position of the 6.2- $\mu\text{m}$  feature are correlated to the stellar effective temperature (p-value  $5 \times 10^{-4}$  and  $4 \times 10^{-3}$  resp.): cool stars display red features.

The correlation between  $T_{\text{eff}}$  and 7.8- $\mu\text{m}$  wavelength position was already found in smaller samples by Sloan et al. (2007), Boersma et al. (2008) and Keller et al. (2008). As we have shown, it holds for a broad variety of pre-main-sequence

stars, with spectral types ranging from M0 to early B. Smolders et al. (2010) have recently extended the correlation to lower  $T_{\text{eff}}$  and redder features with the detection of hydrocarbon emission in S-type AGB stars. The stellar radiation field strongly influences the chemistry of the surrounding hydrocarbon molecules, regardless of the object's evolutionary status or specificities of the circumstellar environment.

Sloan et al. (2007) propose that a red feature indicates the presence of a hydrocarbon mixture with a higher aliphatic/aromatic ratio, an idea that is supported by laboratory measurements (Pino et al. 2008). Here we report a few newly found correlations in our sample of Herbig Ae stars that provide further evidence for this interpretation.

The position and width of the 7.8- $\mu\text{m}$  feature are linked to the effective temperature of the central star. Moreover, the strength of the aromatic 8.6- $\mu\text{m}$  CH in-plane bending mode, relative to the 6.2 and 7.8- $\mu\text{m}$  CC features, and the aliphatic-to-aromatic luminosity ratio<sup>4</sup> depend on  $T_{\text{eff}}$  as well. In fact, all these parameters are interconnected. Table 6 summarizes these correlations. Figs. 15 and 16 show that, while targets with a red 7.8- $\mu\text{m}$  feature (i.e. cool stars) have a low flux ratio of the aromatic 8.6- $\mu\text{m}$  CH and 7.8- $\mu\text{m}$  CC features, they produce fractionally more aliphatic emission. It is clear that illuminated hydrocarbon molecules around stars with different effective temperature are chemically different.

Herbig Ae stars are by nature strong photospheric UV emitters. Because of the rather low accretion rates in most targets, the additional UV excess due to accretion energy dissipation is relatively unimportant for these stars. We can therefore consider the effective temperature as a direct indicator of the stellar UV radiation field.

Strong UV radiation appears to preferentially destroy or convert the aliphatic component in the disks. Photodestruction of the CH bonds is expected from laboratory experiments (e.g., Muñoz Caro et al. 2001). This effect is stronger for aliphatic molecules, as aromatic rings give more stability to the molecule by allowing distri-

<sup>4</sup>This is the ratio of the summed line fluxes of the aliphatic 6.8 and 7.2- $\mu\text{m}$  features with respect to those of the detected PAH features in the covered wavelength range.

bution of the UV-induced excitation energy. This is consistent with the lower line fluxes of the 8.6- $\mu\text{m}$  feature relative to the aliphatic CH features observed in cooler stars. The disappearance of the 6.8 and 7.2- $\mu\text{m}$  features, both linked to CH bonds in aliphatic hydrocarbons, could therefore point to a more rapid dehydrogenation of the aliphatic molecules, rather than a complete removal of this component. However, the experiments of Muñoz Caro et al. (2001) show that the aromatic CH bonds are also eventually destroyed by the UV radiation. The aromatic feature at 8.6  $\mu\text{m}$  should therefore become weaker with increasing UV strength as well. The opposite trend is observed: sources with strong UV fields display a higher aromatic CH/CC flux ratio. We note that this interpretation relies on the identification of the 8.6- $\mu\text{m}$  feature as due to aromatic CH modes. Alternatively, it may be that also aromatic CC modes contribute to its strength. In the latter case, the observations show that the aromatic hydrocarbons undergo structural changes induced by UV field, resulting in Class A features and an increased contribution of CC modes to the 8.6- $\mu\text{m}$  feature.

The observed increase in the aromatic CH strength at higher temperatures is consistent with experimental work by Mennella et al. (2001), who suggest that the heating of carbon grains should reduce the number of aliphatic CH bonds and increase the number of aromatic CH bonds. Also UV irradiance increase the relative degree of aromatic clustering, but in thermal annealing at temperatures above 300 K, this increase is accompanied with a growth of the graphitic clusters. Under UV irradiation, the clusters remain small (Mennella et al. 1998).

In diffuse interstellar clouds, large ( $> 30$  C atoms) PAHs are expected to have normal hydrogen coverage (i.e. one H atom per peripheral C atom; aromatic bond), while very large PAHs may be fully hydrogenated (i.e. two H atoms; aliphatic bond, Le Page et al. 2003). The transition of full to normal hydrogen coverage could occur through UV photolysis of the aliphatic CH bonds and replacement with aromatic CH bonds. This would reduce the aliphatic fingerprint in the infrared spectrum and pump the aromatic CH/CC ratio. Because UV processing keeps the cluster sizes small, thermal annealing may be needed to

grow the clusters and increase the aromatic CH emission strength. The observational trends in our sample then indicate that not only UV photodestruction, but also thermal annealing of carbon grains and hydrogenation in the UV-shielded disk interior, is important in circumstellar disks around Herbig Ae stars.

## 5. Conclusions

In this paper, we have investigated hydrocarbon emission in the Spitzer IRS spectra of a sample of 53 Herbig Ae stars. We find that 70% of the sources display PAH emission, and 55% aliphatic features at 6.8 and/or 7.2  $\mu\text{m}$ . Five targets (9%) display a feature complex at 16–19  $\mu\text{m}$ . Below we list our main conclusions.

- We confirm the correlation between the PAH feature-to-stellar luminosity ratio and the shape of the infrared spectral energy distribution, first mentioned by Meeus et al. (2001). PAHs are a tracer of the gas disk, while the SED probes the thermal dust emission. If the dust and gas disk are colocated, the trend indicates that the illuminated surface of a flared disk is larger than that of a flattened disk. The volume occupied by excited PAHs is therefore larger in the first group. It is suggested in the literature that sources with settled dust disks can nonetheless produce strong PAH emission if their gas disk is still flared and exposed to stellar UV flux. This could explain the existence of the few targets with flattened dust disks but strong PAH emission. However, most targets follow the general trend. We conclude that PAHs in the dust-poor disk atmosphere are either rapidly removed from the gas phase, or that the gas and dust in most disks are well coupled and settle together.
- The stellar radiation field determines the chemistry of the hydrocarbon population in the circumstellar disk. Ranked according to increasing stellar effective temperature, the infrared spectra of Herbig Ae stars show an increase of the aromatic CH emission, but a decrease of the aliphatic CH emission. Aliphatic CH bonds are more easily destroyed than aromatic CH bonds, which

explains the decrease in aliphatic signature. However, this effect cannot explain the increase in the aromatic CH/CC ratio with increasing UV strength. The solution may be found in thermal annealing and the hydrogenation balance of the PAHs. The latter can only influence the PAH chemistry if turbulent vertical mixing is important at the disk's surface, and brings PAH molecules from UV-immersed regions to the disk interior and back.

- The 6.2 and 7.8- $\mu\text{m}$  CC features are redder in cooler stars. The link with the relative strength of the aliphatic features indicates that the wavelength shift indeed is a measure for the aliphatic/aromatic content ratio of the hydrocarbon mixture.
- The strong connection between spectral fingerprint and stellar effective temperature shows that hydrocarbons immediately react to the UV field to which they are exposed. Therefore, the chemistry of hydrocarbon molecules does not in general trace disk evolution. However, the observations indicate that targets with a flattened dust disk harbor hydrocarbons which may be more processed. They appear to have rougher molecular edges and/or are smaller than those in flared dust disks.

We have expanded the knowledge of the chemistry of hydrocarbon molecules in disks. Once irradiated, the free-flying molecules are quickly chemically altered by the stellar UV field and their history is deleted. However, PAHs in disks must have a significant aliphatic component when they appear at the disk surface. Laboratory experiments have shown that the formation of aliphatic ( $\text{CH}_2$ ) groups on the edges of PAH molecules can already occur under very mild conditions (Jäger et al. 2006,  $T \approx 400\text{ K}$ ). Such conditions are available in the warm regions of disks around Herbig Ae stars, which makes it probable that in-situ production and (re-)hydrogenation of the hydrocarbon mixture are processes which take place below the disk surface.

This work is based on observations made with the Spitzer Space Telescope, which is operated by

the Jet Propulsion Laboratory, California Institute of Technology under a contract with NASA. BA thanks Kees Dullemond for helpful discussions.

## REFERENCES

- Acke, B., Min, M., van den Ancker, M. E., et al. 2009, *A&A*, 502, L17
- Acke, B. & van den Ancker, M. E. 2004, *A&A*, 426, 151
- Acke, B., van den Ancker, M. E., Dullemond, C. P., van Boekel, R., & Waters, L. B. F. M. 2004, *A&A*, 422, 621
- Allamandola, L. J., Tielens, G. G. M., & Barker, J. R. 1989, *ApJS*, 71, 733
- Bauschlicher, C. W., Peeters, E., & Allamandola, L. J. 2009, *ApJ*, 697, 311
- Bauschlicher, Jr., C. W., Peeters, E., & Allamandola, L. J. 2008, *ApJ*, 678, 316
- Beintema, D. A., van den Ancker, M. E., Molster, F. J., et al. 1996, *A&A*, 315, L369
- Boersma, C., Bouwman, J., Lahuis, F., et al. 2008, *A&A*, 484, 241
- Bouwman, J., Meeus, G., de Koter, A., et al. 2001, *A&A*, 375, 950
- Bouwman, J., Henning, T., Hillenbrand, L. A., et al. 2008, *ApJ*, 683, 479
- Chiar, J. E., Tielens, A. G. G. M., Whittet, D. C. B., et al. 2000, *ApJ*, 537, 749
- Dartois, E., Geballe, T. R., Pino, T., et al. 2007, *A&A*, 463, 635
- Dullemond, C. P. & Dominik, C. 2004a, *A&A*, 417, 159
- Dullemond, C. P. & Dominik, C. 2004b, *A&A*, 421, 1075
- Dullemond, C. P., Dominik, C., & Natta, A. 2001, *ApJ*, 560, 957
- Dullemond, C. P., Henning, Th., Visser, R., et al. 2007, *A&A*, 473, 457
- Fedele, D., van den Ancker, M. E., Acke, B., et al. 2008, *A&A*, 491, 809
- Furlan, E., Watson, D. M., McClure, M. K., et al. 2009, *ApJ*, 703, 1964
- Furton, D. G., Laiho, J. W., & Witt, A. N. 1999, *ApJ*, 526, 752
- Gielen, C., van Winckel, H., Matsuura, M., et al. 2009, *A&A*, 503, 843
- Habart, E., Natta, A., & Krügel, E. 2004, *A&A*, 427, 179
- Henning, T. & Meeus, G. 2009, arXiv:0911.1010
- Henning, T. & Salama, F. 1998, *Science*, 282, 2204
- Hony, S., Van Kerckhoven, C., Peeters, E., et al. 2001, *A&A*, 370, 1030
- Houck, J. R., Roellig, T. L., van Cleve, J., et al. 2004, *ApJS*, 154, 18
- Hudgins, D. M., Bauschlicher, Jr., C. W., & Allamandola, L. J. 2005, *ApJ*, 632, 316
- Jäger, C., Krasnokutski, S., Staicu, A., et al. 2006, *ApJS*, 166, 557
- Keller, L. D., Sloan, G. C., Forrest, W. J., et al. 2008, *ApJ*, 684, 411
- Kendall, M. 1938, *Biometrika*, 30 (1-2), 81
- Kessler, M. F., Steinz, J. A., Anderegg, M. E., et al. 1996, *A&A*, 315, L27
- Kurucz, R. L. 1991, *BAAS*, 23, 1047
- Le Page, V., Snow, T. P., & Bierbaum, V. M. 2003, *ApJ*, 584, 316
- Li, A. & Draine, B. T. 2002, *ApJ*, 572, 232
- Mann, H. B. & Whitney, D. R. 1947, *Annals of Mathematical Statistics*, 18, 50
- Mattioda, A. L., Allamandola, L. J., & Hudgins, D. M. 2005a, *ApJ*, 629, 1183
- Mattioda, A. L., Hudgins, D. M., & Allamandola, L. J. 2005b, *ApJ*, 629, 1188
- Meeus, G., Waters, L. B. F. M., Bouwman, J., et al. 2001, *A&A*, 365, 476
- Meijer, J., Dominik, C., de Koter, A., et al. 2008, *A&A*, 492, 451
- Mennella, V., Colangeli, L., Bussoletti, E., Palumbo, P., & Rotundi, A. 1998, *ApJ*, 507, L177

Mennella, V., Muñoz Caro, G. M., Ruiterkamp, R., et al. 2001, *A&A*, 367, 355

Muñoz Caro, G. M., Ruiterkamp, R., Schutte, W. A., Greenberg, J. M., & Mennella, V. 2001, *A&A*, 367, 347

Peeters, E., Hony, S., Van Kerckhoven, C., et al. 2002, *A&A*, 390, 1089

Peeters, E., Mattioda, A. L., Hudgins, D. M., & Allamandola, L. J. 2004, *ApJ*, 617, L65

Pino, T., Dartois, E., Cao, A., et al. 2008, *A&A*, 490, 665

Sargent, B. A., Forrest, W. J., Tayrien, C., et al. 2009, *ApJ*, 690, 1193

Sellgren, K., Uchida, K. I., & Werner, M. W. 2007, *ApJ*, 659, 1338

Sloan, G. C. 2008, in *IAU Symposium*, Vol. 251, *IAU Symposium*, ed. S. Kwok & S. Sandford, 191–194

Sloan, G. C., Jura, M., Duley, W. W., et al. 2007, *ApJ*, 664, 1144

Sloan, G. C., Keller, L. D., Forrest, W. J., et al. 2005, *ApJ*, 632, 956

Smolders, K., Acke, B., Verhoelst, T., et al. 2010, *A&A*, 514, L1+

Sturm, E., Lutz, D., Tran, D., et al. 2000, *A&A*, 358, 481

Tielens, A. G. G. M. 2008, *ARA&A*, 46, 289

van Boekel, R., Min, M., Waters, L. B. F. M., et al. 2005, *A&A*, 437, 189

van der Plas, G., van den Ancker, M. E., Fedele, D., et al. 2008, *A&A*, 485, 487

Van Kerckhoven, C., Hony, S., Peeters, E., et al. 2000, *A&A*, 357, 1013

Verhoeff, A. P., Min, M., Acke, B., et al. 2010, *arXiv:1004.2208*

Werner, M. W., Roellig, T. L., Low, F. J., et al. 2004a, *ApJS*, 154, 1

Werner, M. W., Uchida, K. I., Sellgren, K., et al. 2004b, *ApJS*, 154, 309

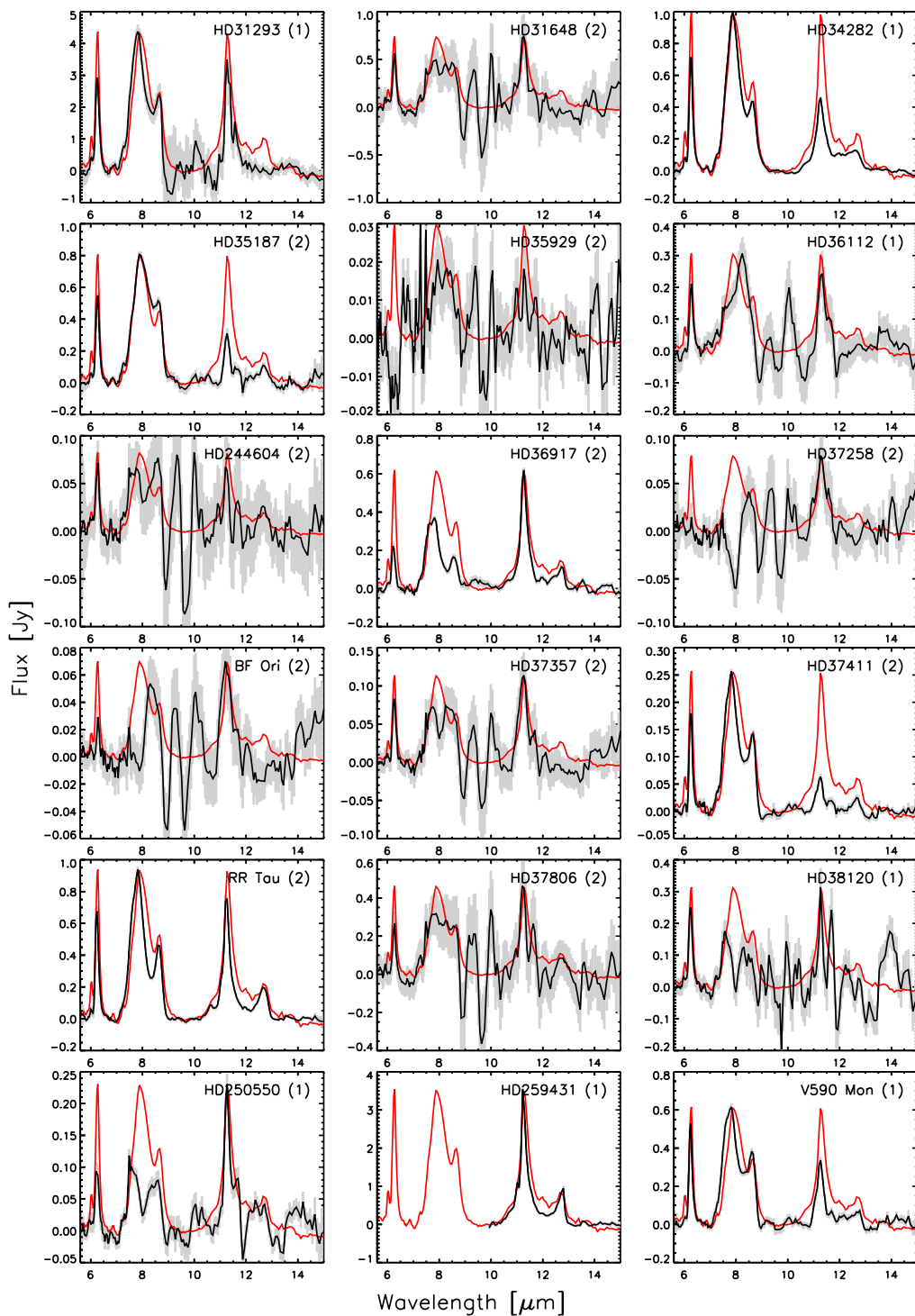


Fig. 1.— Residual PAH spectra. Next to the source name, the Meeus group classification is indicated. As a reference, the PAH spectrum of HD 169142 is overplotted in red, scaled to the peak of the residual spectrum.

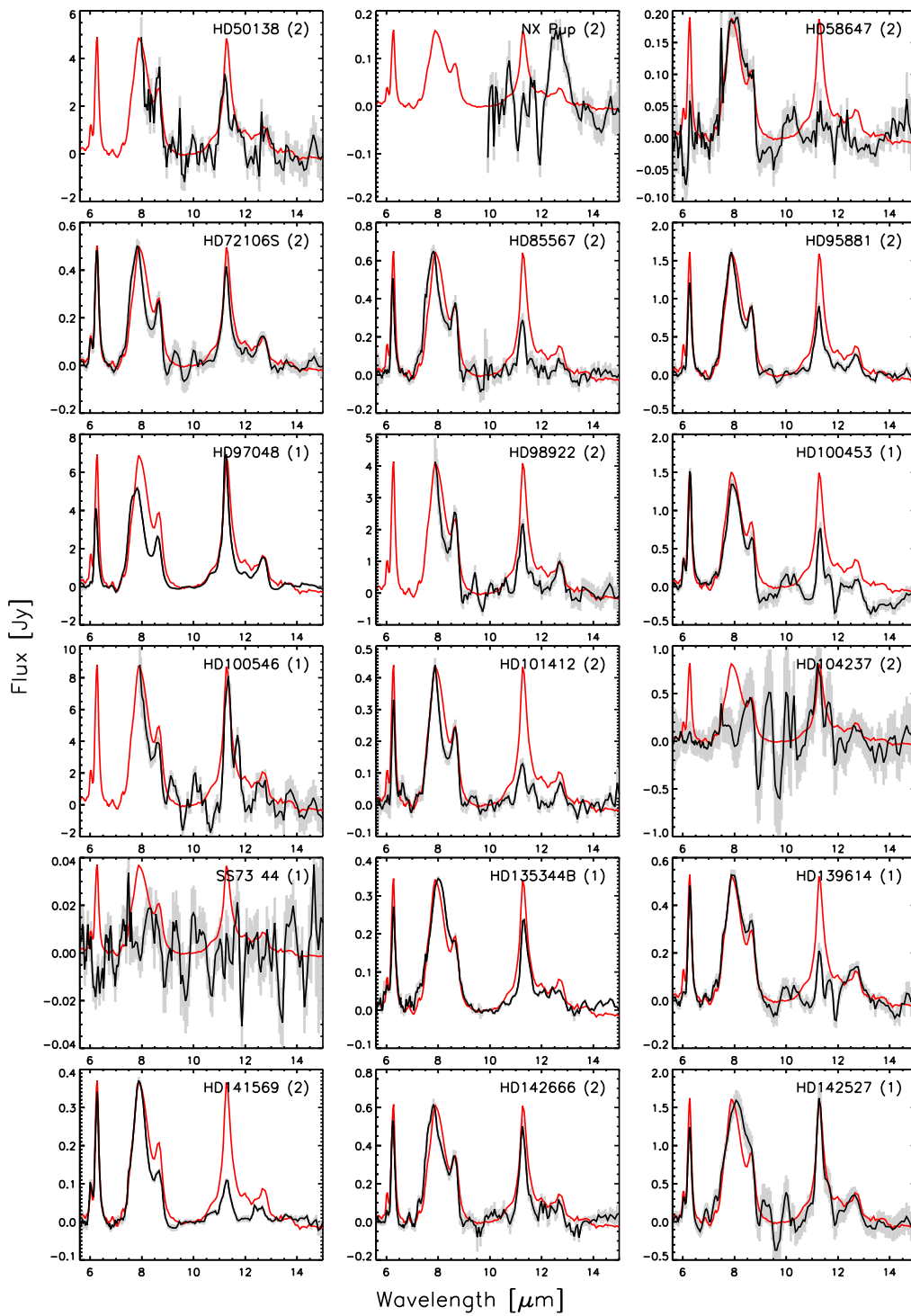


Fig. 1.— Cont'd.

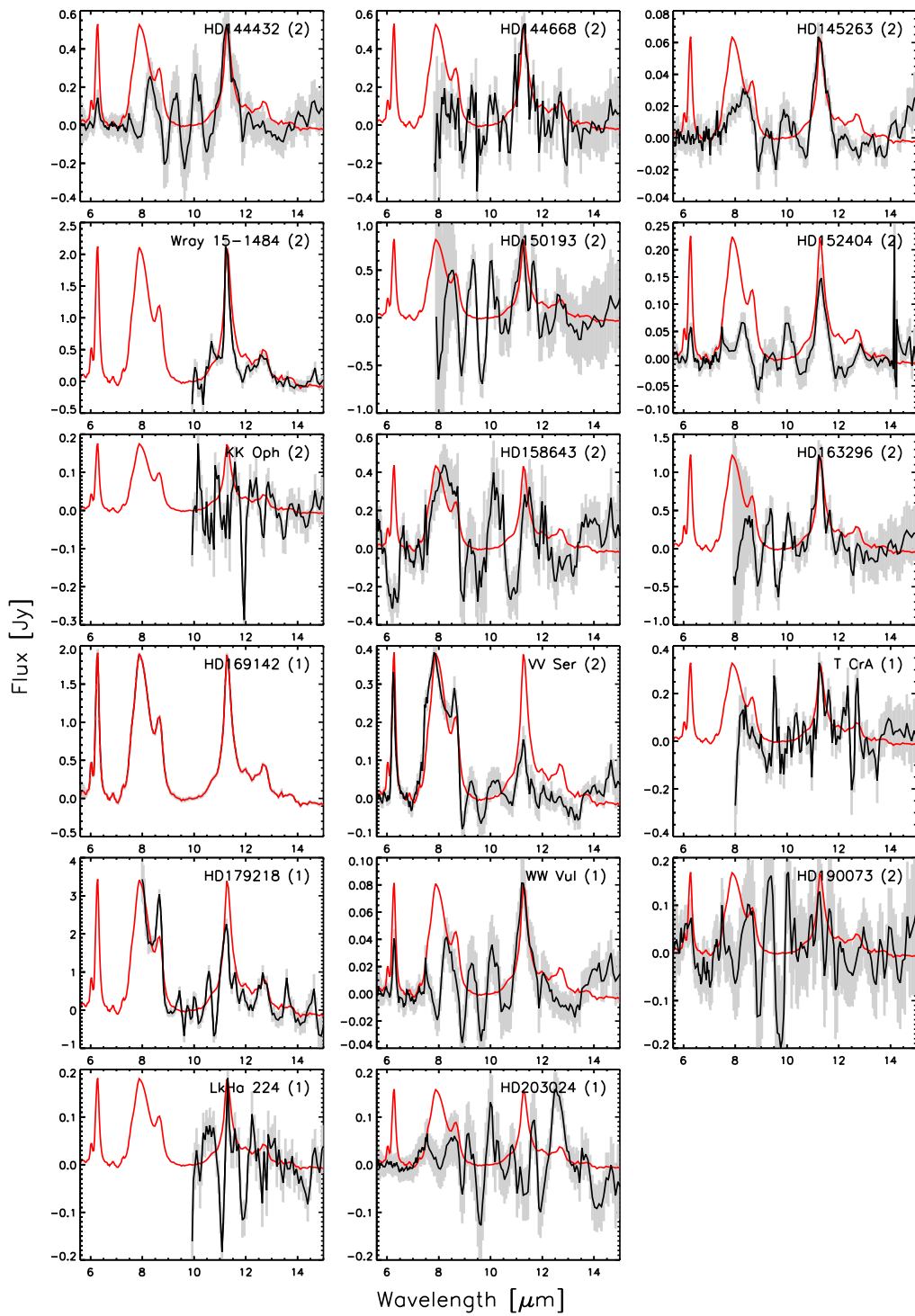


Fig. 1.— Cont'd.



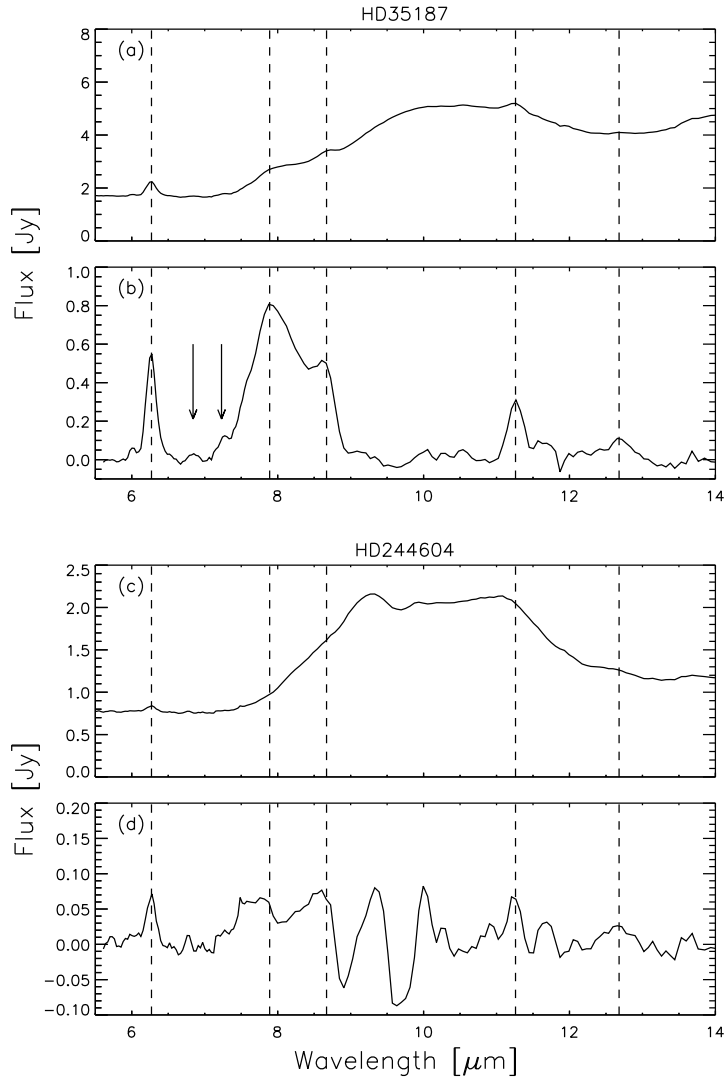


Fig. 2.— (a) Spitzer IRS spectrum of HD 35187 and (b) PAH spectrum, extracted by subtracting the best fit to the dust and continuum (J10). The major features at 6.2, 7.8, 8.6, 11.3 and 12.7  $\mu\text{m}$  are clearly visible (dashed lines), as well as the aliphatic features at 6.8 and 7.2  $\mu\text{m}$  (arrows). (c) Spitzer IRS spectrum of HD 244604 and (d) PAH spectrum. Residuals of the silicate dust fit are present on a few-percent level and hamper a reliable detection of the (weak) PAH features longward of 7  $\mu\text{m}$ .

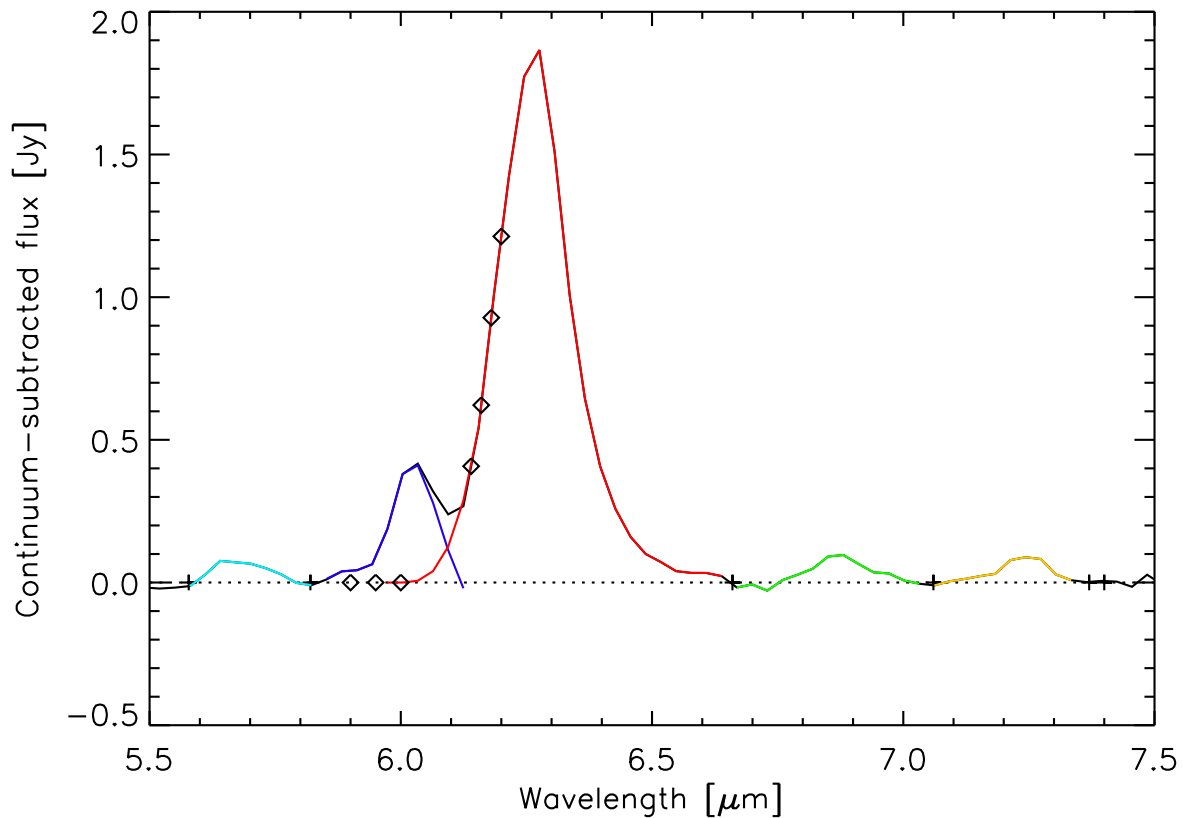


Fig. 3.— Extraction of the features in the 6- $\mu\text{m}$  range of the IRS spectrum of HD 169142. A continuum spline, through the anchor points indicated with +, was subtracted. The 5.7, 6.8 and 7.2- $\mu\text{m}$  features are not blended and can be measured directly. A spline is fitted to the blue wing of the large 6.2- $\mu\text{m}$  feature at well-chosen wavelength positions (diamonds). It is assumed that the large feature reaches the continuum level (i.e. zero) at 6  $\mu\text{m}$ . The resulting line profiles (colored lines) are plotted on top of the original spectrum (black). See text for details.

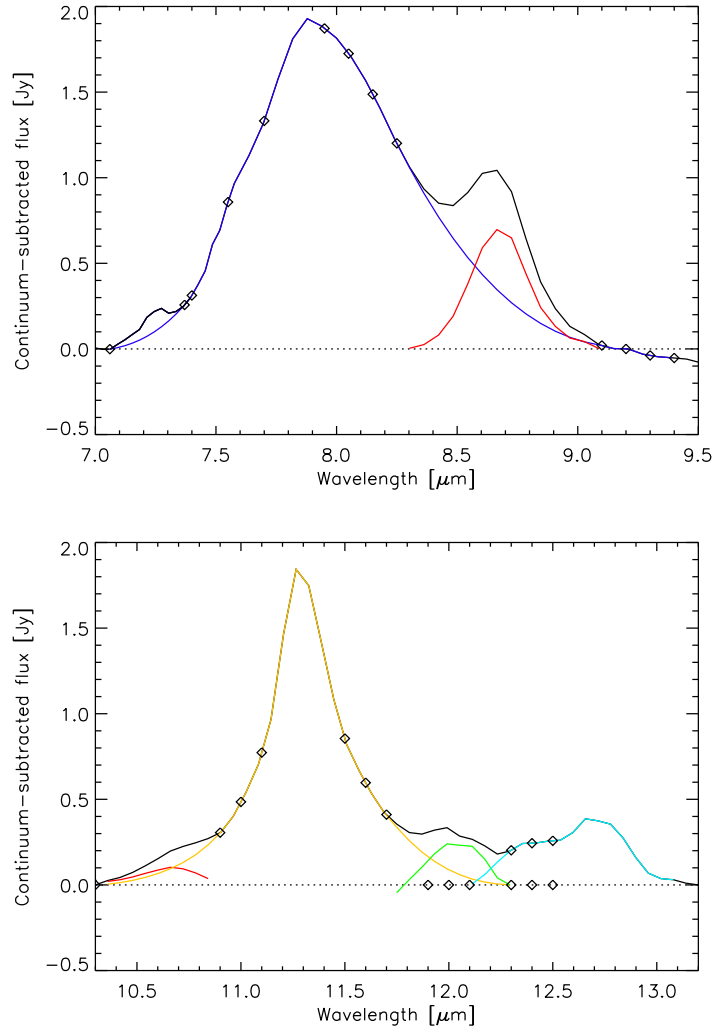


Fig. 4.— Extraction of the features in the 7–9- $\mu\text{m}$  range (*top*) of the residual PAH spectrum of HD 169142. Splines are fitted a priori fixed anchor wavelengths (diamonds). The resulting line profiles (colored lines) are plotted on top of the original spectrum (black). Note that the 7.2- $\mu\text{m}$  feature is extracted, considering the 7.8- $\mu\text{m}$  feature as continuum emission (see also Fig. 3). *Bottom*: Extraction of the features in the 10–13- $\mu\text{m}$  region.

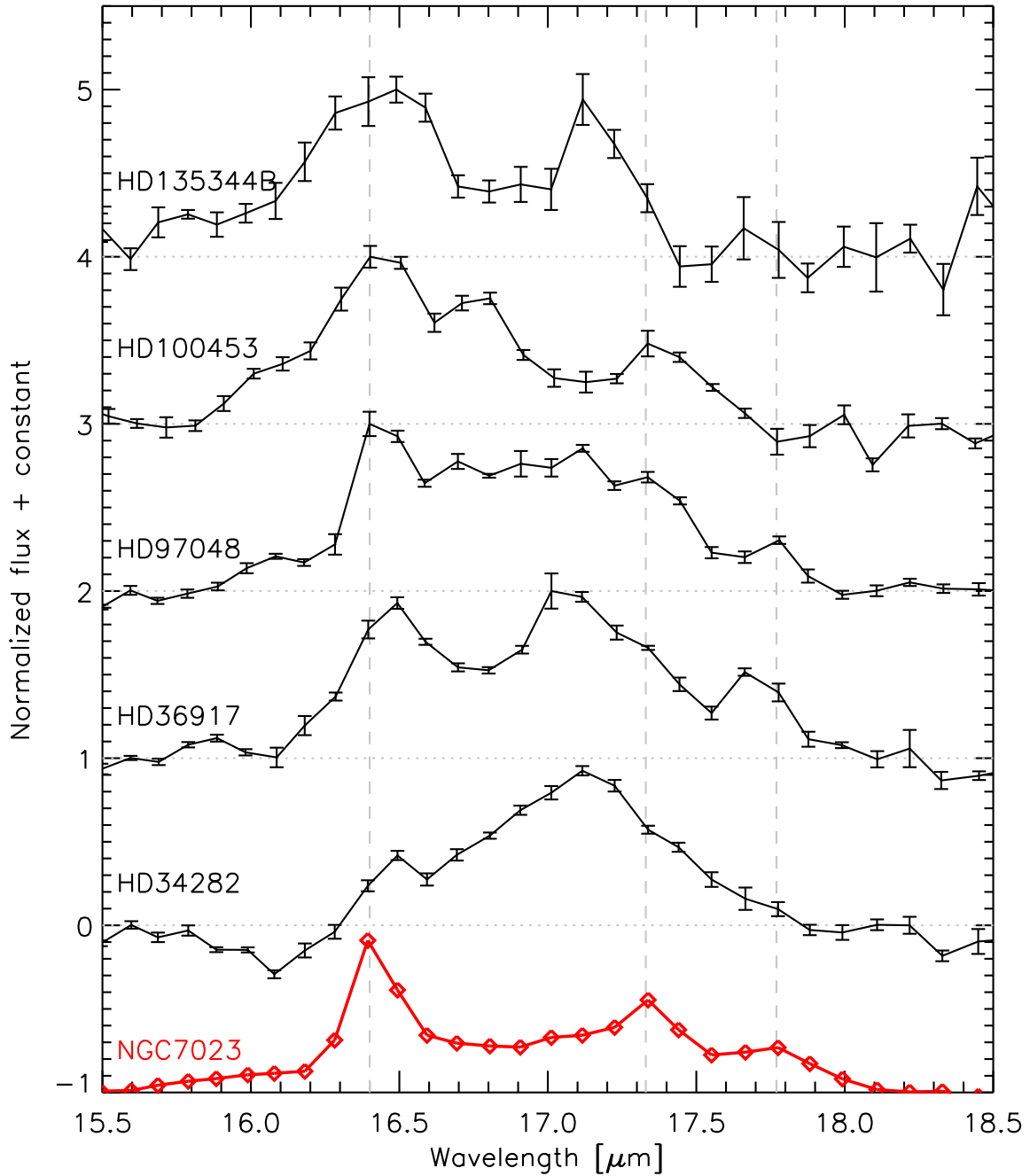


Fig. 5.— Detected features of the skeletal CCC out-of-plane bending mode. The spectrum of the NGC 7023 reflection nebula is shown at the bottom as a reference (Sellgren et al. 2007). It is rebinned to a lower resolution of 160 to allow direct comparison with the Herbig Ae spectra. The full vertical line indicates the position of the  $\text{H}_2$  0-0 S(1) molecular line. Even if it would be present, confusion with the broad PAH feature can be excluded.

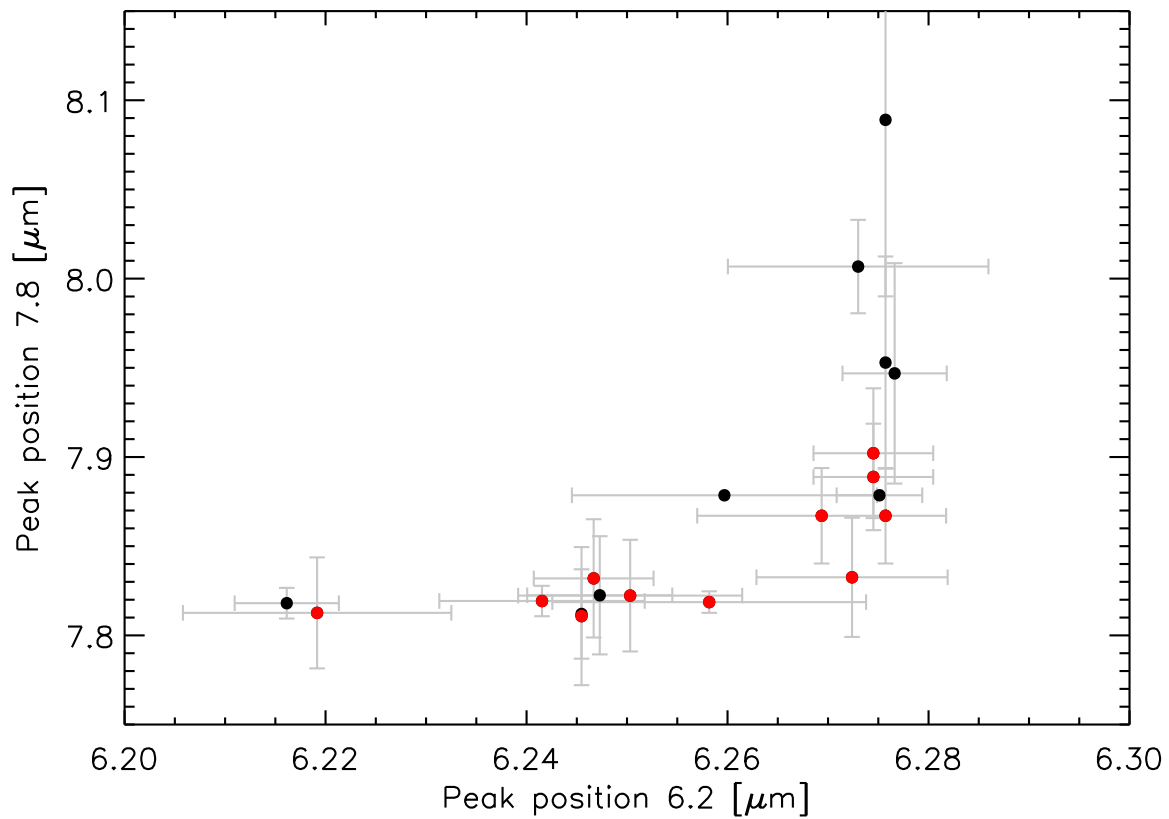


Fig. 6.— The peak position of the 6.2 and 7.8- $\mu\text{m}$  features (p-value  $3 \times 10^{-5}$ ). The black dots represent group I sources, the red group II. This convention is used throughout the entire paper.

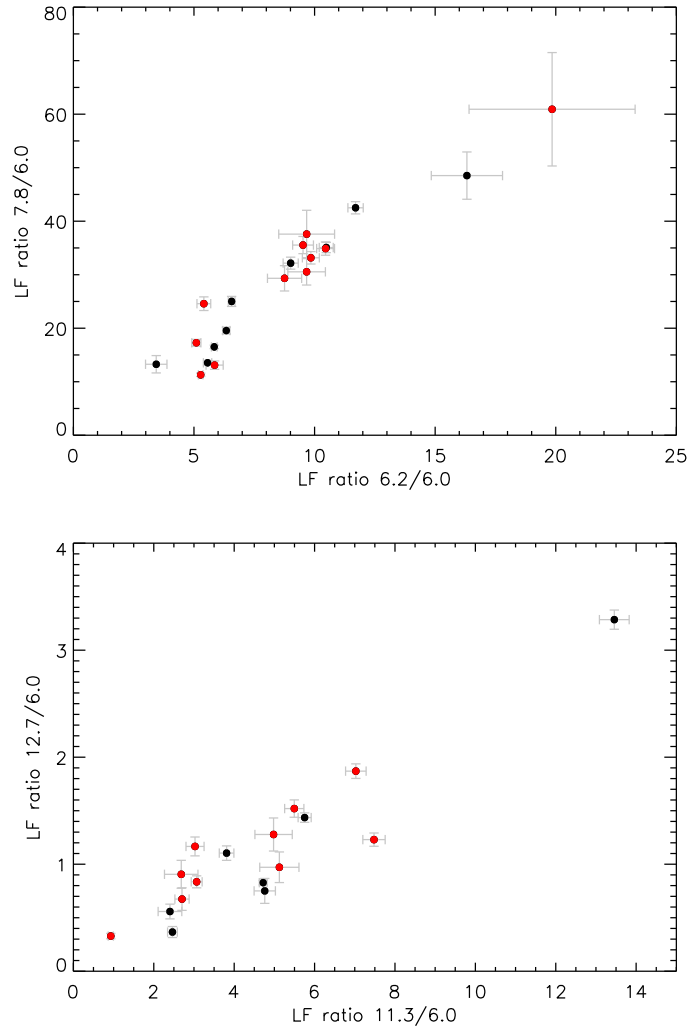


Fig. 7.— Strong correlation between the line flux ratios 6.2/6.0 and 7.8/6.0 (p-value  $1 \times 10^{-6}$ , *top*) and 12.7/6.0 and 11.3/6.0 (p-value  $2 \times 10^{-4}$ , *bottom*). The 6.2 and 7.8- $\mu\text{m}$  features are both CC stretching modes, the 11.3 and 12.7- $\mu\text{m}$  features are due to CH out-of-plane bending modes.

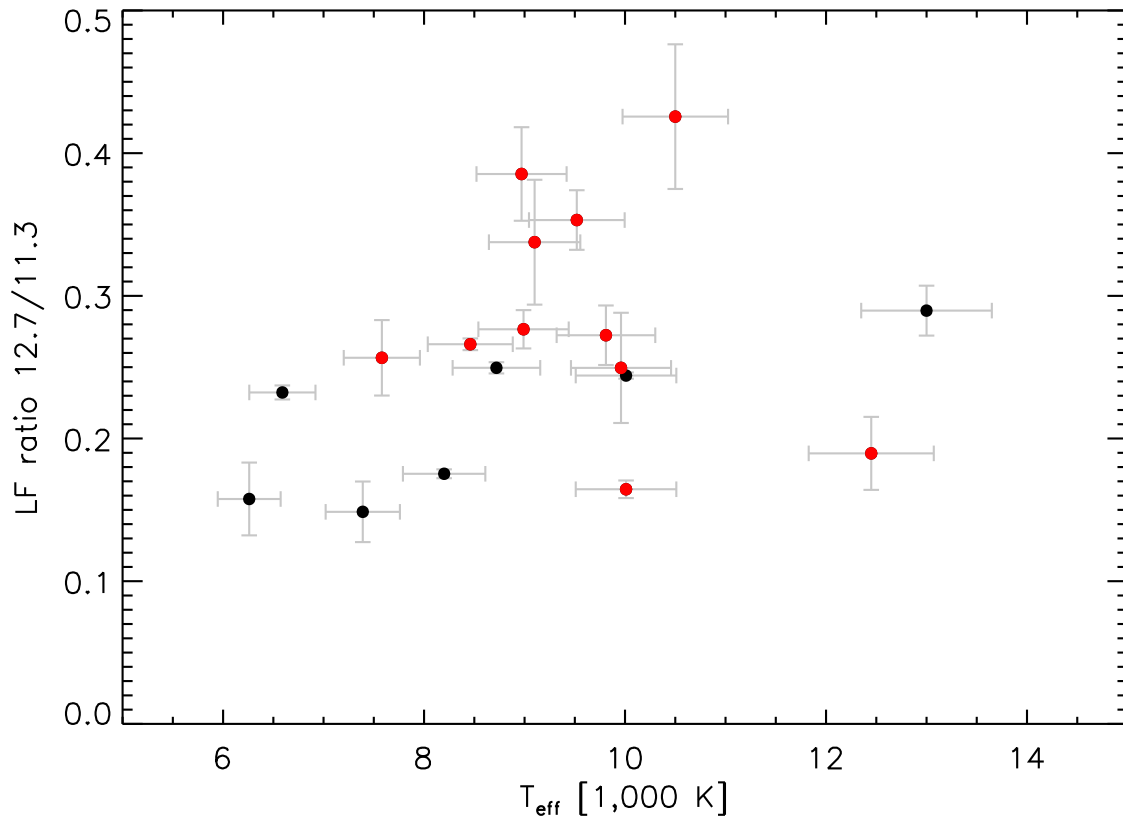


Fig. 8.— Line flux ratio of the CH out-of-plane bending features at 12.7 (duo+trio CH) and 11.3- $\mu\text{m}$  (solo CH) as a function of stellar effective temperature. A correlation including all sample targets can be excluded (p-value 15%), but is tentatively present for the group I sources alone (p-value 5%).

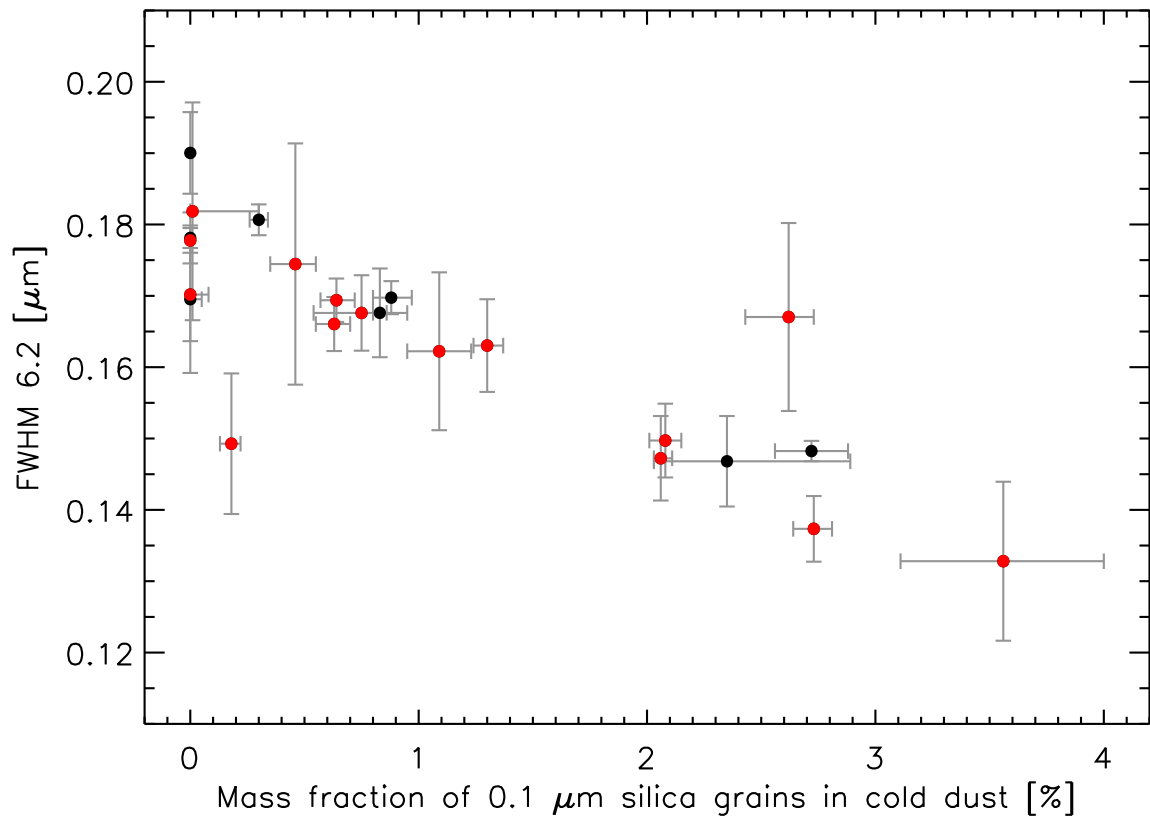


Fig. 9.— Correlation between the FWHM of the PAH 6.2- $\mu\text{m}$  feature versus the mass fraction of the 0.1- $\mu\text{m}$  silica grains in the cold dust component (p-value  $1 \times 10^{-5}$ ).



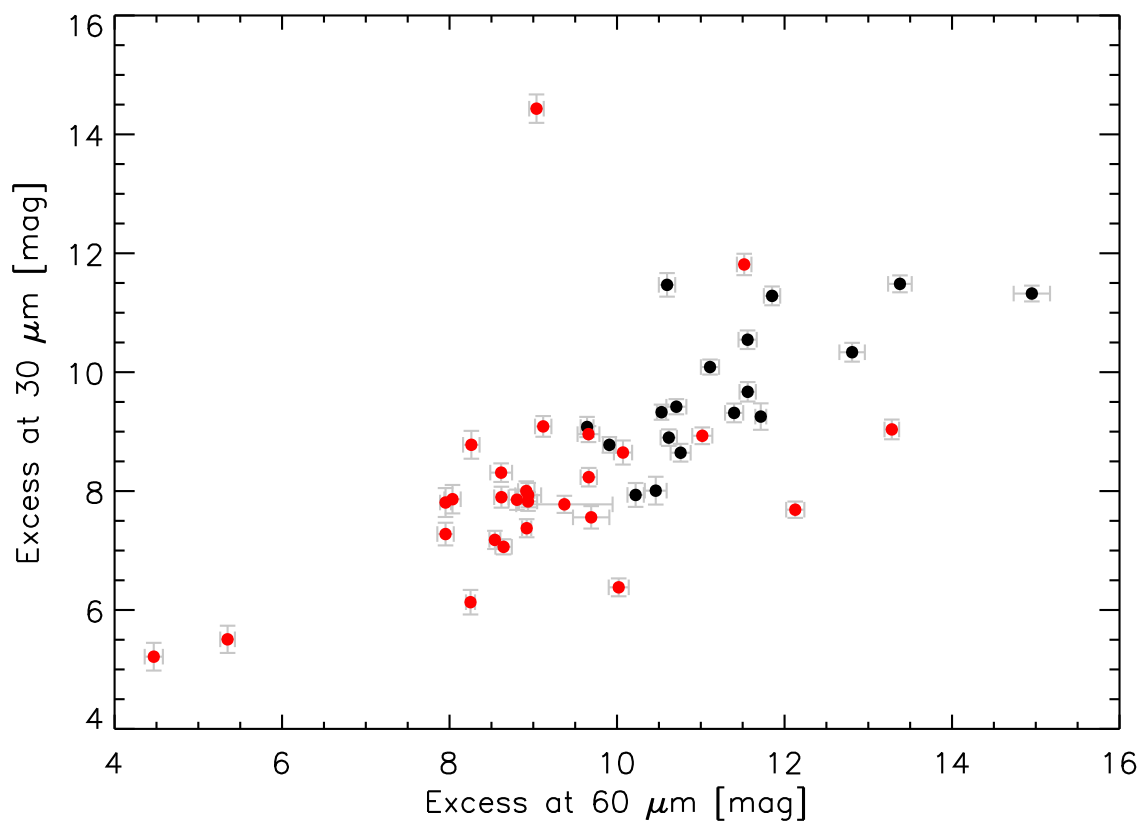


Fig. 10.— The excess magnitude at 30 and 60  $\mu\text{m}$ . Both are strongly connected (p-value  $2 \times 10^{-7}$ ).

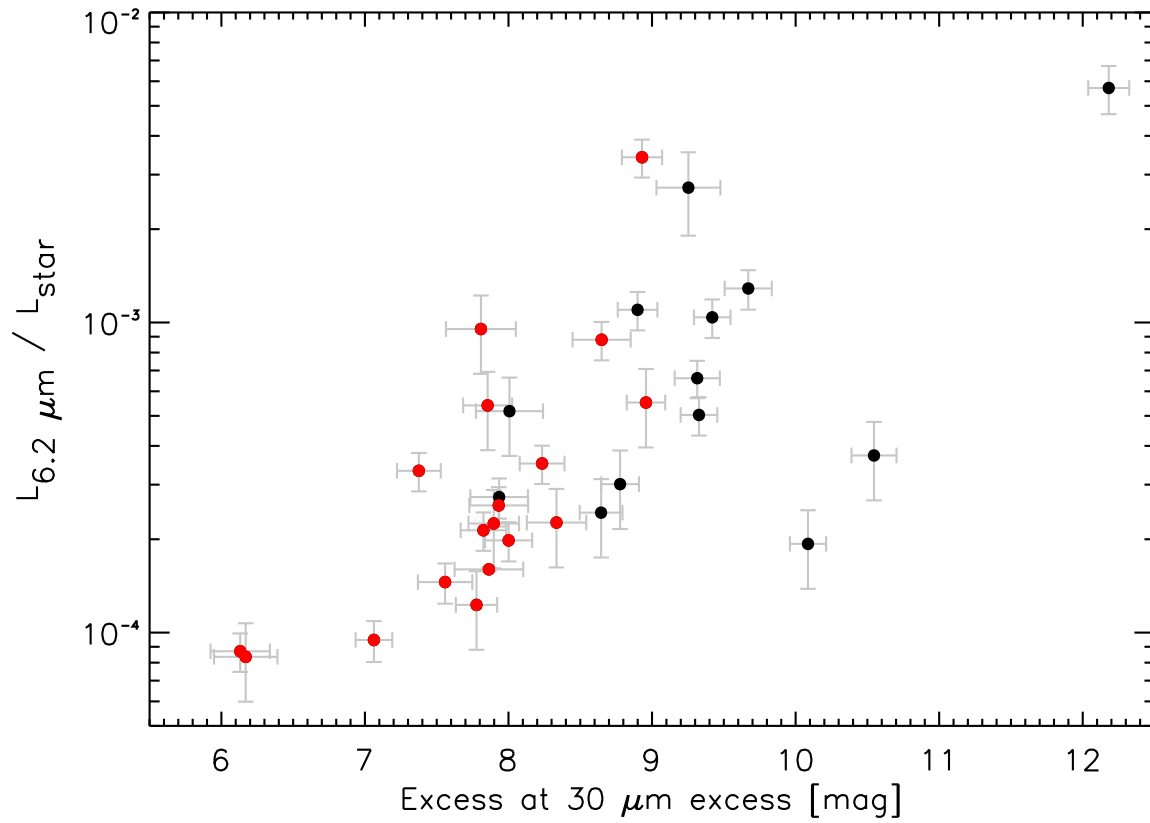


Fig. 11.— The luminosity ratio of the PAH 6.2- $\mu\text{m}$  CC stretch feature and the central star increases with increasing excess at 30- $\mu\text{m}$  (p-value  $4 \times 10^{-5}$ ).

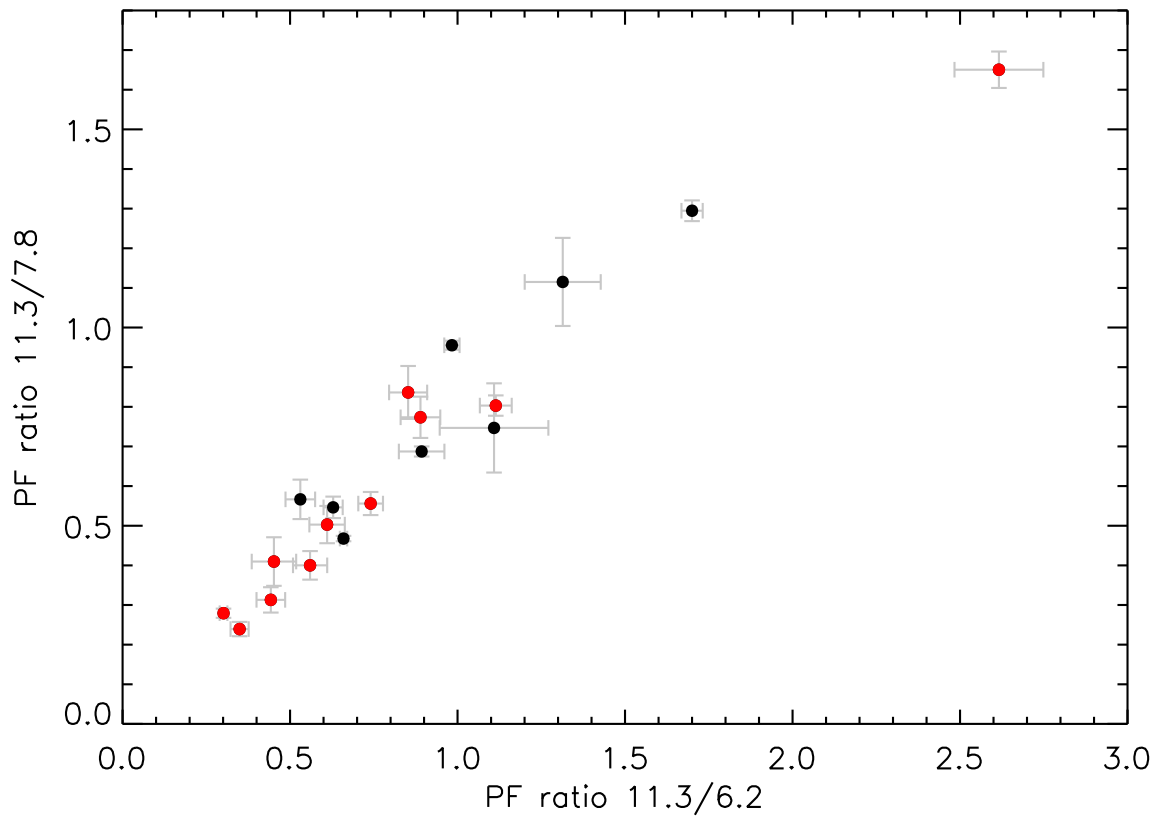


Fig. 12.— Correlation between the peak flux ratios 11.3/6.2 and 11.3/7.8 (p-value  $2 \times 10^{-6}$ ). Note that the group II sources (red dots) have lower values than group I sources (black) for both ratios.

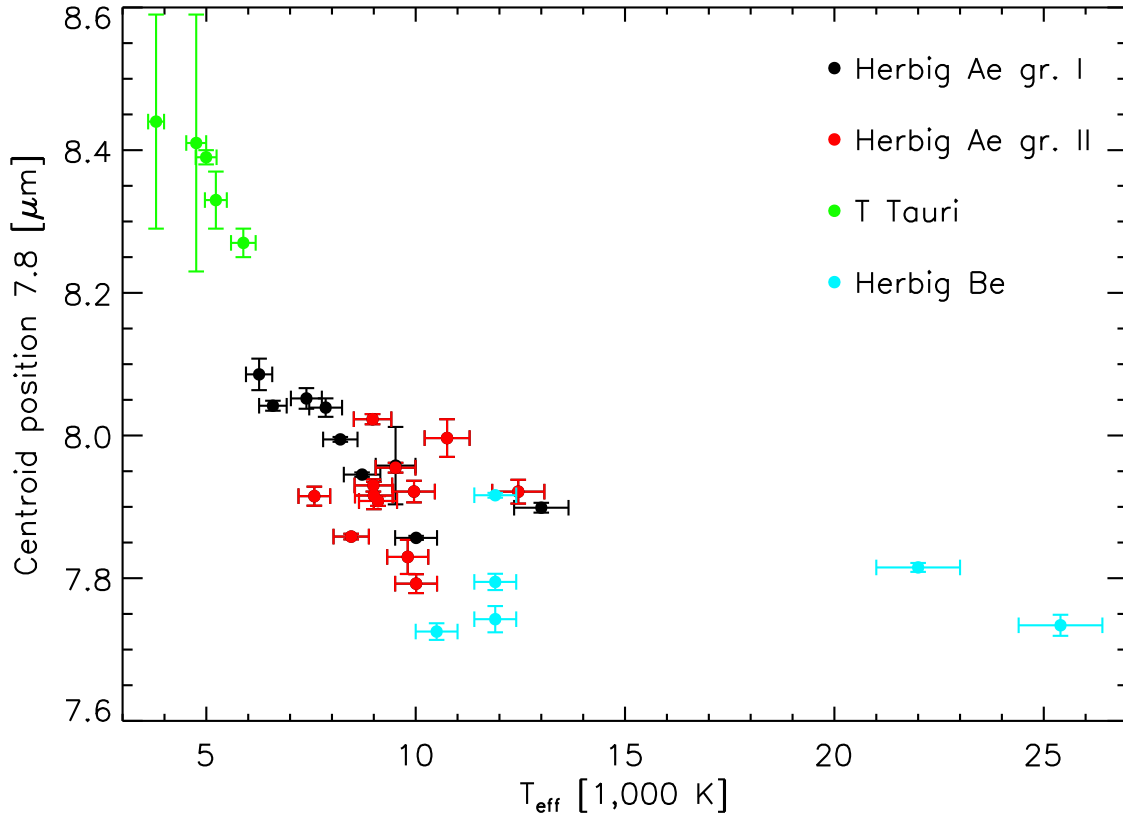


Fig. 13.— The centroid position of the 7.8- $\mu\text{m}$  feature decreases with increasing stellar effective temperature. We have included the T Tauri stars with detected PAH emission from Bouwman et al. (2008). The Herbig Be stars were observed under Spitzer program PID 50180. The correlation is significant for the Herbig Ae stars alone (p-value  $4 \times 10^{-3}$ ) and even more so for the entire sample of young stars (p-value  $7 \times 10^{-8}$ ).

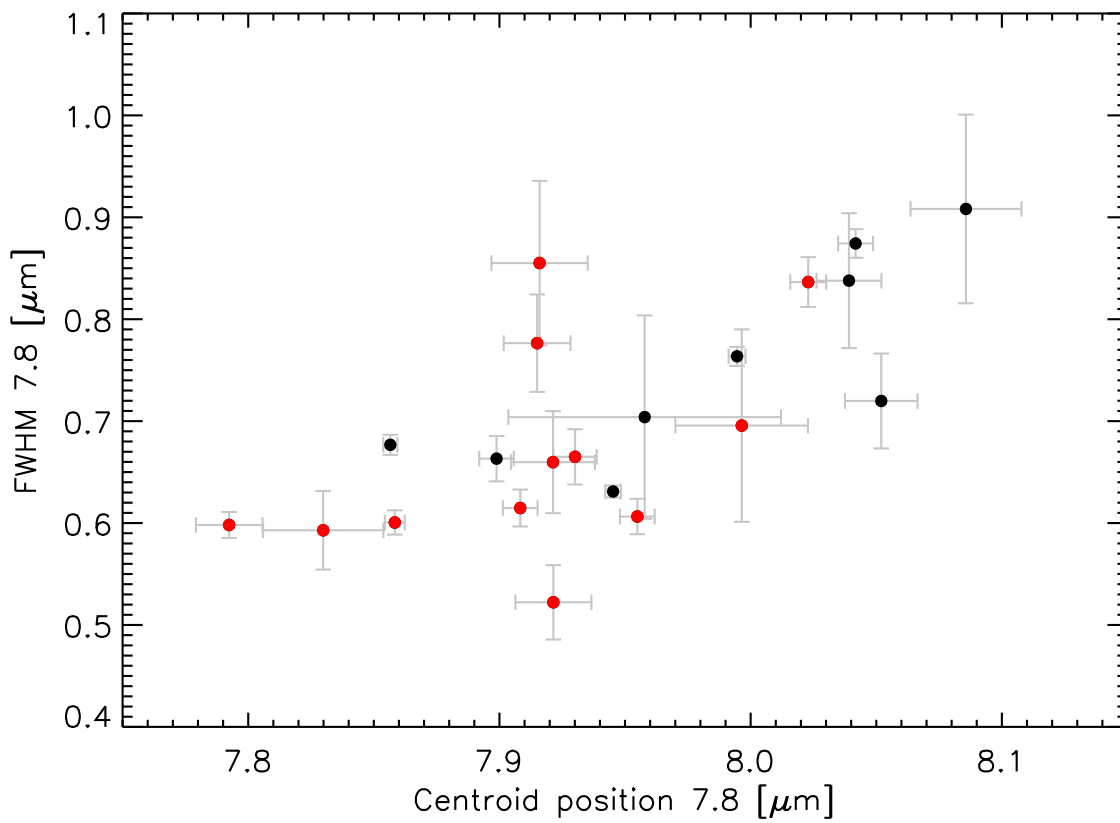


Fig. 14.— A red 7.8- $\mu\text{m}$  feature has a larger FWHM (p-value  $2 \times 10^{-3}$ ).

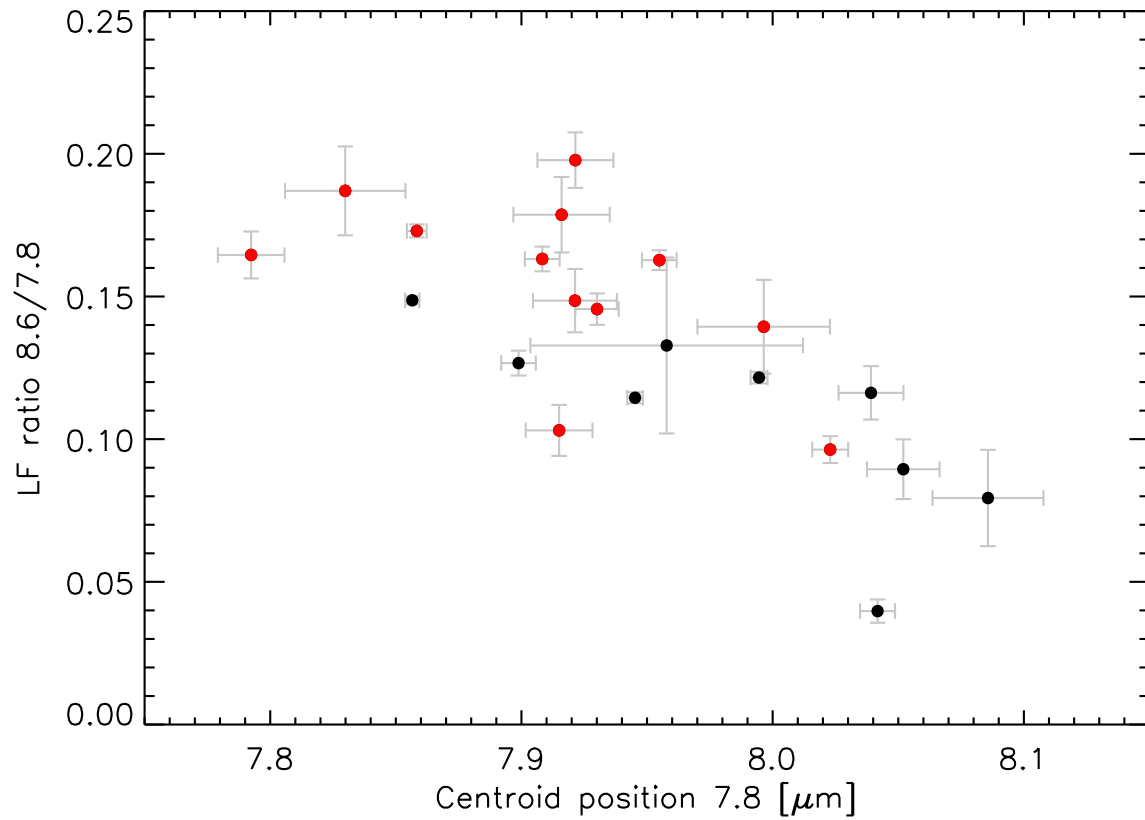


Fig. 15.— When the centroid wavelength of the 7.8- $\mu\text{m}$  feature increases, the 8.6/7.8 line flux ratio decreases (p-value  $4 \times 10^{-4}$ ). The 7.8- $\mu\text{m}$  feature is due to CC stretches, the 8.6- $\mu\text{m}$  feature is attributed to a CH in-plane bending mode in aromatic hydrocarbons.

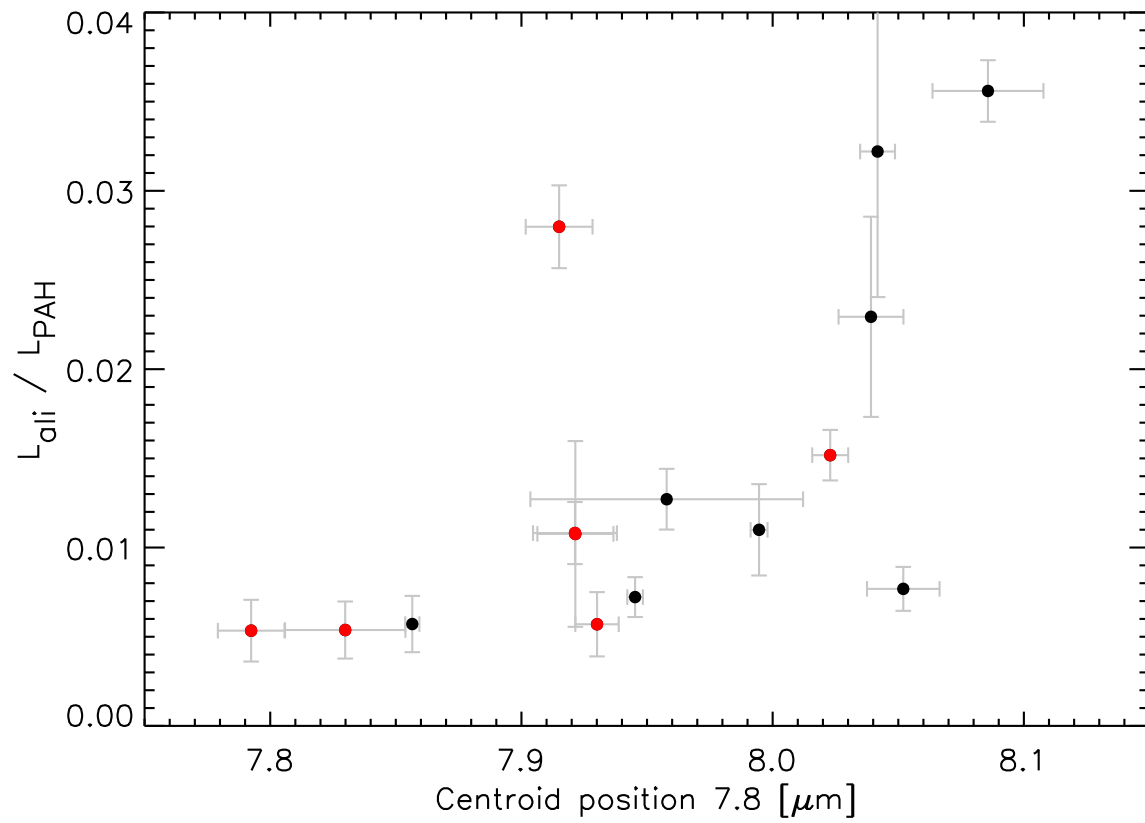


Fig. 16.— Correlation between the aliphatic-to-PAH luminosity ratio and the centroid position of the 7.8- $\mu\text{m}$  feature (p-value  $4 \times 10^{-3}$ ).

TABLE 1  
STELLAR AND DISK PARAMETERS

Target	Group	$T_{\text{eff}}$ (K)	$M(7\ \mu\text{m})^a$ (mag)	$M(30\ \mu\text{m})^a$ (mag)	$[13.5/7]^b$	$[30/13.5]^b$
HD 31293	I	9520	4.3±0.1	9.3±0.2	1.14±0.05	4.5±0.1
HD 31648	II	8720	4.6±0.1	8.2±0.2	1.28±0.03	1.19±0.03
HD 34282	I	8720	4.1±0.1	9.3±0.2	0.56±0.09	10.0±0.6
HD 35187	II	8970	2.8±0.1	7.8±0.2	2.5±0.2	2.1±0.1
HD 35929	II	6870	2.0±0.1	3.9±0.2	0.70±0.03	0.43±0.01
HD 36112	I	7850	3.6±0.1	8.6±0.1	1.37±0.05	4.1±0.2
HD 244604	II	8730	3.8±0.1	7.9±0.2	1.51±0.05	1.43±0.03
HD 36917	II	10010	2.8±0.1	6.2±0.2	0.86±0.06	1.35±0.06
HD 37258	II	8970	4.1±0.1	7.9±0.2	1.65±0.04	1.10±0.03
BF Ori	II	8985	4.2±0.1	7.6±0.2	1.36±0.03	0.87±0.03
HD 37357	II	9230	3.3±0.1	7.8±0.1	1.70±0.06	1.85±0.04
HD 37411	II	9100	4.1±0.1	9.0±0.1	1.12±0.08	4.0±0.2
RR Tau	II	8460	5.0±0.1	8.9±0.1	1.1±0.1	1.72±0.04
HD 37806	II	9480	5.1±0.1	8.3±0.2	1.25±0.03	0.85±0.07
HD 38120	I	10500	4.7±0.1	10.5±0.2	4.5±0.5	2.6±0.2
HD 250550	I	10700	5.0±0.1	10.1±0.1	2.2±0.1	2.5±0.1
HD 259431	I	25400	—	10.3±0.2	—	2.55±0.05
V590 Mon	I	13000	6.8±0.1	12.2±0.1	3.0±0.6	2.2±0.1
HD 50138	II	12230	—	14.4±0.2	—	0.78±0.04
NX Pup	II	7290	—	11.8±0.2	—	0.78±0.02
HD 58647	II	10750	3.6±0.1	5.5±0.2	0.66±0.02	0.49±0.01
HD 72106S	II	9810	3.4±0.1	7.9±0.2	2.0±0.2	1.62±0.07
HD 85567	II	12450	4.9±0.1	7.9±0.2	1.02±0.02	0.82±0.04
HD 95881	II	8990	4.9±0.1	7.8±0.2	1.00±0.03	0.77±0.05
HD 97048	I	10010	3.9±0.1	9.7±0.2	1.6±0.4	5.9±0.4
HD 98922	II	10500	—	8.8±0.2	—	0.75±0.03
HD 100453	I	7390	3.9±0.1	9.4±0.1	1.7±0.1	5.2±0.3
HD 100546	I	10500	—	11.3±0.2	—	3.5±0.2
HD 101412	II	9960	4.6±0.1	7.9±0.2	1.31±0.04	0.92±0.03
HD 104237	II	8405	3.4±0.1	7.2±0.2	1.31±0.02	1.28±0.03
SS73 44	I	15000	6.6±0.1	11.5±0.1	2.10±0.09	2.40±0.08
HD 135344B	I	6590	3.4±0.1	7.9±0.2	0.32±0.02	10.9±0.3
HD 139614	I	7850	3.0±0.1	9.3±0.1	4.1±0.3	4.2±0.3
HD 141569	II	9520	1.1±0.1	6.1±0.2	0.73±0.07	6.8±0.2
HD 142666	II	7580	3.3±0.1	7.4±0.2	1.45±0.06	1.53±0.05
HD 142527	I	6260	3.1±0.1	8.0±0.2	0.95±0.02	5.0±0.1
HD 144432	II	7345	3.5±0.1	8.0±0.2	1.82±0.06	1.82±0.06
HD 144668	II	7930	—	8.3±0.2	—	0.96±0.02
HD 145263	II	7200	0.8±0.2	5.4±0.2	1.9±0.1	2.0±0.1
Wray 15-1484	II	30000	—	9.0±0.2	—	0.76±0.02
HD 150193	II	8990	—	9.1±0.2	—	1.42±0.05
HD 152404	II	6450	2.5±0.1	7.1±0.1	1.13±0.05	3.3±0.1
KK Oph	II	8030	—	7.7±0.1	—	1.04±0.02
HD 158643	II	10100	2.7±0.1	5.2±0.2	0.96±0.02	0.59±0.02
HD 163296	II	8720	—	6.4±0.2	—	2.0±0.1
HD 169142	I	8200	2.8±0.1	8.9±0.1	1.7±0.3	7.8±0.5
VV Ser	II	9000	5.7±0.1	8.6±0.2	1.09±0.02	0.79±0.02
T CrA	I	7200	—	11.3±0.1	—	5.0±0.3
HD 179218	I	9810	—	11.5±0.2	—	2.4±0.2
WW Vul	I	8430	4.4±0.1	8.8±0.1	1.80±0.05	1.60±0.04
HD 190073	II	8990	4.3±0.1	7.3±0.2	1.14±0.02	0.75±0.02
LkHa 224	I	7850	—	8.9±0.1	—	1.99±0.02
HD 203024	I	8200	3.2±0.1	9.1±0.2	5.0±0.6	2.3±0.2

NOTE.—(a) The excess magnitude  $M(\lambda)$  is relative to the stellar photosphere at  $\lambda$ ; (b) Continuum flux ratio at the given wavelengths.



TABLE 2  
SAMPLE-AVERAGED PARAMETERS OF THE DETECTED FEATURES

Feature	Limits ( $\mu\text{m}$ )	Mode	Ref.	Det. (%)	$\langle\text{PP}\rangle$ ( $\mu\text{m}$ )	$\langle\text{Cen}\rangle$ ( $\mu\text{m}$ )	$\langle\text{FWHM}\rangle$ ( $\mu\text{m}$ )	$\langle\log_{10} L_f/L_\star\rangle$	$\langle\log_{10} L_f/L_{\text{PAH}}\rangle$
5.7	5.58–5.83	CH-oop?	1	45	$5.69 \pm 0.02$	$5.70 \pm 0.02$	$0.07 \pm 0.02$	$-4.8 \pm 0.6$	$-2.2 \pm 0.3$
6.0	5.83–6.10	carbonyl-s?	1	78	$6.00 \pm 0.04$	$6.00 \pm 0.03$	$0.11 \pm 0.02$	$-4.2 \pm 0.4$	$-1.5 \pm 0.3$
6.2	5.83–6.66	CC-s (PANH?)	1,5	78	$6.26 \pm 0.02$	$6.28 \pm 0.02$	$0.16 \pm 0.01$	$-3.4 \pm 0.5$	$-0.7 \pm 0.2$
6.8	6.66–7.06	CH <sub>2</sub> and CH <sub>3</sub> (ali) or CH-ip n	2 5	38	$6.87 \pm 0.03$	$6.85 \pm 0.07$	$0.11 \pm 0.04$	$-4.7 \pm 0.3$	$-2.0 \pm 0.3$
7.2	7.06–7.36	CH <sub>3</sub> (ali)	2	50	$7.22 \pm 0.02$	$7.22 \pm 0.01$	$0.11 \pm 0.03$	$-4.6 \pm 0.2$	$-2.0 \pm 0.3$
7.8	7.06–9.10	CC-s	1,5	53	$7.88 \pm 0.08$	$7.94 \pm 0.08$	$0.7 \pm 0.1$	$-2.8 \pm 0.6$	$-0.24 \pm 0.06$
8.6	8.25–9.10	CH-ip	1,5	50	$8.66 \pm 0.03$	$8.64 \pm 0.03$	$0.25 \pm 0.04$	$-3.7 \pm 0.6$	$-1.1 \pm 0.2$
10.6	10.35–10.90	CH-oop s +	3	26	$10.64 \pm 0.04$	$10.61 \pm 0.06$	$0.25 \pm 0.09$	$-4.5 \pm 0.7$	$-2.1 \pm 0.3$
11.3	10.35–12.30	CH-oop s n(-)	3,5	42	$11.27 \pm 0.02$	$11.3 \pm 0.1$	$0.29 \pm 0.05$	$-3.6 \pm 0.5$	$-1.0 \pm 0.2$
12.0	11.70–12.30	CH-oop d n+-	3	28	$12.03 \pm 0.05$	$12.00 \pm 0.03$	$0.22 \pm 0.08$	$-4.5 \pm 0.6$	$-1.9 \pm 0.3$
12.7	12.10–13.10	CH-oop dt n+-	3,5	38	$12.7 \pm 0.1$	$12.61 \pm 0.05$	$0.41 \pm 0.09$	$-4.2 \pm 0.6$	$-1.7 \pm 0.1$
13.5	13.20–13.90	CH-oop q n+-	3,5	19	$13.59 \pm 0.04$	$13.6 \pm 0.1$	$0.19 \pm 0.07$	$-5.2 \pm 0.5$	$-2.7 \pm 0.4$
16–19	15.60–18.10	CCC-oop	4	9	$16.7 \pm 0.4$	$16.8 \pm 0.3$	$0.8 \pm 0.3$	$-4.0 \pm 0.5$	$-1.6 \pm 0.4$

NOTE.—The error bar represents the standard deviation in the sample. Det. = detection rate; PP = Peak position; Cen = Centroid position; FWHM = Full width at half maximum;  $L_f/L_\star$  = Feature-to-stellar luminosity ratio;  $L_f/L_{\text{PAH}}$  = Feature-to-total-PAH luminosity ratio. The integration limits of the features are given in the second column. The third column summarizes the identification of the mode of the feature, as published in the literature. CH = carbon-hydrogen bond; CC = carbon-carbon bond. oop = out-of-plane bending mode; ip = in-plane bending or wagging mode; s = stretching mode. PANH = nitrogenated PAH; ali = aliphatic. For the features in the 10 – 14- $\mu\text{m}$  region: s = solo or non-adjacent CH group; d = duo; t = trio; q = quartet CH group; n = neutral PAHs; + = cationic PAHs; - = anionic PAHs.

References. — (1) Peeters et al. 2002; (2) Dartois et al. 2007; (3) Hony et al. 2001; (4) Peeters et al. 2004; (5) Bauschlicher et al. 2009.

TABLE 3  
LINE FLUXES OF THE PAH AND ALIPHATIC FEATURES IN THE 5–10- $\mu$ M RANGE

Target	5.7	6.0	6.2	6.8	7.2	7.8	8.6
HD 31293	<5 (-13)	72±1 (-13)	475±4 (-13)	24±4 (-13)	15±2 (-13)	181±6 (-12)	24±6 (-12)
HD 31648	<7 (-13)	224±9 (-14)	90±1 (-13)	8±3 (-13)	92±8 (-14)	<2 (-11)	<5 (-12)
HD 34282	3±1 (-13)	96±3 (-14)	1010±5 (-14)	17±4 (-14)	25±5 (-14)	3380±8 (-14)	387±6 (-14)
HD 35187	7±4 (-14)	88±4 (-14)	839±6 (-14)	35±5 (-14)	37±5 (-14)	313±2 (-13)	30±1 (-13)
HD 35929	<1 (-13)	<7 (-14)	<1 (-13)	<4 (-13)	<1 (-13)	<5 (-13)	<2 (-13)
HD 36112	12±9 (-14)	41±6 (-14)	414±7 (-14)	36±7 (-14)	3±1 (-13)	<1 (-11)	<1 (-12)
HD 244604	<2 (-13)	37±3 (-14)	148±3 (-14)	<1 (-13)	<8 (-14)	<2 (-12)	<9 (-13)
HD 36917	8±3 (-14)	71±3 (-14)	364±4 (-14)	14±5 (-14)	<4 (-13)	123±1 (-13)	20±1 (-13)
HD 37258	<2 (-13)	<9 (-14)	<1 (-13)	<2 (-13)	<9 (-14)	<7 (-13)	<5 (-13)
BF Ori	<9 (-14)	11±1 (-14)	61±3 (-14)	<6 (-14)	<8 (-14)	<1 (-12)	<4 (-13)
HD 37357	<9 (-14)	24±2 (-14)	129±3 (-14)	9±5 (-14)	<2 (-13)	<3 (-12)	<6 (-13)
HD 37411	11±2 (-14)	24±3 (-14)	235±4 (-14)	<9 (-14)	<7 (-14)	912±6 (-14)	149±4 (-14)
RR Tau	48±7 (-14)	94±3 (-14)	922±8 (-14)	<1 (-13)	<2 (-13)	311±1 (-13)	537±7 (-14)
HD 37806	<5 (-13)	89±6 (-14)	479±9 (-14)	<4 (-13)	81±8 (-14)	<1 (-11)	<6 (-13)
HD 38120	<1 (-13)	59±6 (-14)	412±8 (-14)	19±7 (-14)	29±7 (-14)	<7 (-12)	<1 (-12)
HD 250550	9±3 (-14)	37±3 (-14)	166±3 (-14)	15±8 (-14)	21±2 (-14)	<6 (-12)	<3 (-13)
HD 259431	n.s.	n.s.	n.s.	n.s.	n.s.	n.s.	n.s.
V590 Mon	<2 (-13)	76±3 (-14)	681±4 (-14)	<2 (-13)	<3 (-13)	243±2 (-13)	31±1 (-13)
HD 50138	n.s.	n.s.	n.s.	n.s.	n.s.	n.s.	<8 (-12)
NX Pup	n.s.	n.s.	n.s.	n.s.	n.s.	n.s.	n.s.
HD 58647	<9 (-13)	<4 (-13)	<5 (-13)	<6 (-13)	<6 (-13)	83±2 (-13)	12±1 (-13)
HD 72106S	29±5 (-14)	144±3 (-14)	759±3 (-14)	<2 (-13)	19±6 (-14)	162±3 (-13)	30±2 (-13)
HD 85567	2±1 (-13)	76±6 (-14)	73±1 (-13)	<5 (-13)	43±7 (-14)	232±4 (-13)	34±3 (-13)
HD 95881	7±1 (-13)	163±6 (-14)	170±1 (-13)	<6 (-13)	6±2 (-13)	569±5 (-13)	83±3 (-13)
HD 97048	30±4 (-13)	47±1 (-13)	551±3 (-13)	15±3 (-13)	7±5 (-13)	2001±7 (-13)	297±3 (-13)
HD 98922	n.s.	n.s.	n.s.	n.s.	n.s.	n.s.	21±1 (-12)
HD 100453	11±1 (-13)	39±1 (-13)	214±2 (-13)	<9 (-13)	7±1 (-13)	522±7 (-13)	47±5 (-13)
HD 100546	n.s.	n.s.	n.s.	n.s.	n.s.	n.s.	23±2 (-12)
HD 101412	<2 (-13)	56±3 (-14)	301±6 (-14)	<5 (-13)	2±1 (-13)	137±2 (-13)	27±1 (-13)
HD 104237	<6 (-13)	<3 (-13)	<4 (-13)	<7 (-13)	<4 (-13)	<8 (-12)	<6 (-12)
SS73 44	<1 (-13)	<1 (-13)	<1 (-13)	<1 (-13)	<9 (-14)	<8 (-13)	<2 (-13)
HD 135344B	2±1 (-13)	11±1 (-13)	37±2 (-13)	4±2 (-13)	33±7 (-14)	1433±9 (-14)	57±6 (-14)
HD 139614	<5 (-13)	44±4 (-14)	712±5 (-14)	4±2 (-13)	45±8 (-14)	212±3 (-13)	25±2 (-13)
HD 141569	11±5 (-14)	89±5 (-14)	524±6 (-14)	<8 (-14)	<1 (-13)	1172±8 (-14)	191±4 (-14)
HD 142666	20±8 (-14)	84±7 (-14)	73±1 (-13)	73±7 (-14)	43±6 (-14)	245±3 (-13)	25±2 (-13)
HD 142527	8±2 (-13)	339±8 (-14)	215±1 (-13)	28±2 (-13)	14±1 (-13)	66±1 (-12)	5±1 (-12)
HD 144432	16±7 (-14)	47±5 (-14)	306±9 (-14)	3±1 (-13)	42±5 (-14)	<3 (-12)	<2 (-12)
HD 144668	n.s.	n.s.	n.s.	n.s.	n.s.	n.s.	<2 (-12)
HD 145263	<2 (-13)	<6 (-14)	<1 (-13)	<7 (-14)	<1 (-13)	<1 (-12)	<2 (-13)
Wray 15-1484	n.s.	n.s.	n.s.	n.s.	n.s.	n.s.	n.s.
HD 150193	n.s.	n.s.	n.s.	n.s.	n.s.	n.s.	<9 (-12)
HD 152404	<2 (-13)	15±4 (-14)	129±5 (-14)	<2 (-13)	<2 (-13)	<1 (-12)	<4 (-13)
KK Oph	n.s.	n.s.	n.s.	n.s.	n.s.	n.s.	n.s.
HD 158643	<2 (-12)	<1 (-12)	<1 (-12)	<3 (-12)	<8 (-13)	<2 (-11)	<3 (-12)
HD 163296	n.s.	n.s.	n.s.	n.s.	n.s.	n.s.	<9 (-12)
HD 169142	10±2 (-13)	442±9 (-14)	258±2 (-13)	9±3 (-13)	67±9 (-14)	729±2 (-13)	89±1 (-13)
VV Ser	<5 (-13)	25±4 (-14)	497±6 (-14)	<1 (-13)	<2 (-13)	153±3 (-13)	27±2 (-13)
T CrA	n.s.	n.s.	n.s.	n.s.	n.s.	n.s.	<9 (-13)
HD 179218	n.s.	n.s.	n.s.	n.s.	n.s.	n.s.	243±8 (-13)
WW Vul	<6 (-14)	12±1 (-14)	79±1 (-14)	<7 (-14)	<4 (-14)	<6 (-13)	<3 (-13)
HD 190073	<2 (-13)	<2 (-13)	<2 (-13)	<5 (-13)	<2 (-13)	<3 (-12)	<2 (-12)
LkHa 224	n.s.	n.s.	n.s.	n.s.	n.s.	n.s.	n.s.
HD 203024	<2 (-13)	<8 (-14)	<1 (-13)	<2 (-13)	<1 (-13)	<4 (-12)	<1 (-12)

NOTE.—The line fluxes and errors are in  $\text{ergs cm}^{-2} \text{s}^{-1}$ , with  $a(b)$  representing  $a \times 10^b$ . For non-detections, the 3-sigma upper limit is given. n.s. = No spectrum available at this wavelength.

TABLE 4  
LINE FLUXES OF THE PAH FEATURES IN THE 10-14  $\mu\text{M}$  RANGE.

Target	10.6	11.3	12.0	12.7	13.5
HD 31293	<5 (-12)	11 $\pm$ 3 (-12)	8 $\pm$ 7 (-13)	<2 (-12)	6 $\pm$ 5 (-13)
HD 31648	<2 (-12)	<7 (-12)	<2 (-12)	<2 (-12)	<1 (-12)
HD 34282	39 $\pm$ 2 (-14)	554 $\pm$ 4 (-14)	89 $\pm$ 2 (-14)	138 $\pm$ 2 (-14)	5 $\pm$ 2 (-14)
HD 35187	11 $\pm$ 8 (-14)	27 $\pm$ 2 (-13)	<3 (-13)	103 $\pm$ 6 (-14)	<2 (-13)
HD 35929	<8 (-14)	<1 (-13)	<7 (-14)	<6 (-14)	<6 (-14)
HD 36112	<7 (-13)	<2 (-12)	<5 (-13)	<4 (-13)	<3 (-13)
HD 244604	<4 (-13)	<7 (-13)	<4 (-13)	<3 (-13)	<3 (-13)
HD 36917	27 $\pm$ 3 (-14)	534 $\pm$ 6 (-14)	59 $\pm$ 3 (-14)	88 $\pm$ 3 (-14)	20 $\pm$ 3 (-14)
HD 37258	<2 (-13)	<9 (-13)	<2 (-13)	<2 (-13)	<1 (-13)
BF Ori	<2 (-13)	<9 (-13)	<2 (-13)	<2 (-13)	<1 (-13)
HD 37357	<3 (-13)	<2 (-12)	<2 (-13)	<2 (-13)	<2 (-13)
HD 37411	<4 (-14)	65 $\pm$ 7 (-14)	<5 (-14)	22 $\pm$ 2 (-14)	<5 (-14)
RR Tau	81 $\pm$ 3 (-14)	658 $\pm$ 7 (-14)	41 $\pm$ 2 (-14)	175 $\pm$ 2 (-14)	7 $\pm$ 2 (-14)
HD 37806	<1 (-12)	<9 (-12)	<1 (-12)	<1 (-12)	<9 (-13)
HD 38120	<6 (-13)	<1 (-12)	<5 (-13)	<6 (-13)	<4 (-13)
HD 250550	<1 (-13)	<9 (-13)	<1 (-13)	<3 (-13)	<1 (-13)
HD 259431	34 $\pm$ 1 (-13)	308 $\pm$ 3 (-13)	240 $\pm$ 8 (-14)	73 $\pm$ 1 (-13)	44 $\pm$ 7 (-14)
V590 Mon	51 $\pm$ 5 (-14)	29 $\pm$ 1 (-13)	<1 (-13)	83 $\pm$ 4 (-14)	<1 (-13)
HD 50138	<3 (-12)	<3 (-11)	<4 (-12)	<1 (-11)	<5 (-12)
NX Pup	<6 (-13)	<5 (-13)	<2 (-13)	<3 (-13)	<2 (-13)
HD 58647	<2 (-13)	<3 (-13)	<2 (-13)	<1 (-13)	<1 (-13)
HD 72106S	<3 (-13)	44 $\pm$ 2 (-13)	43 $\pm$ 9 (-14)	120 $\pm$ 8 (-14)	<2 (-13)
HD 85567	<3 (-13)	39 $\pm$ 2 (-13)	5 $\pm$ 1 (-13)	74 $\pm$ 9 (-14)	<2 (-13)
HD 95881	14 $\pm$ 1 (-13)	90 $\pm$ 2 (-13)	8 $\pm$ 1 (-13)	25 $\pm$ 1 (-13)	<3 (-13)
HD 97048	45 $\pm$ 2 (-13)	633 $\pm$ 4 (-13)	57 $\pm$ 1 (-13)	1547 $\pm$ 9 (-14)	18 $\pm$ 1 (-13)
HD 98922	59 $\pm$ 5 (-13)	18 $\pm$ 1 (-12)	23 $\pm$ 5 (-13)	75 $\pm$ 8 (-13)	<2 (-12)
HD 100453	<7 (-13)	95 $\pm$ 4 (-13)	<7 (-13)	14 $\pm$ 2 (-13)	<5 (-13)
HD 100546	<5 (-12)	<6 (-11)	<5 (-12)	<1 (-11)	<7 (-12)
HD 101412	<2 (-13)	151 $\pm$ 7 (-14)	<1 (-13)	38 $\pm$ 6 (-14)	<1 (-13)
HD 104237	<3 (-12)	<9 (-12)	<2 (-12)	<2 (-12)	<2 (-12)
SS73 44	<9 (-14)	<2 (-13)	<8 (-14)	<9 (-14)	<9 (-14)
HD 135344B	<4 (-14)	260 $\pm$ 3 (-14)	48 $\pm$ 1 (-14)	60 $\pm$ 1 (-14)	10 $\pm$ 2 (-14)
HD 139614	<3 (-13)	<5 (-13)	<3 (-13)	<1 (-12)	<2 (-13)
HD 141569	12 $\pm$ 2 (-14)	83 $\pm$ 3 (-14)	11 $\pm$ 2 (-14)	29 $\pm$ 1 (-14)	4 $\pm$ 1 (-14)
HD 142666	2 $\pm$ 1 (-13)	42 $\pm$ 2 (-13)	82 $\pm$ 9 (-14)	11 $\pm$ 1 (-13)	<2 (-13)
HD 142527	<2 (-12)	161 $\pm$ 8 (-13)	<1 (-12)	25 $\pm$ 4 (-13)	<1 (-12)
HD 144432	<1 (-12)	<7 (-12)	<9 (-13)	<8 (-13)	<7 (-13)
HD 144668	<7 (-13)	<9 (-12)	<9 (-13)	<1 (-12)	<1 (-12)
HD 145263	<7 (-14)	<6 (-13)	<6 (-14)	<5 (-14)	<5 (-14)
Wray 15-1484	33 $\pm$ 4 (-13)	212 $\pm$ 6 (-13)	25 $\pm$ 3 (-13)	52 $\pm$ 3 (-13)	6 $\pm$ 2 (-13)
HD 150193	<2 (-12)	<1 (-11)	<2 (-12)	<3 (-12)	<3 (-12)
HD 152404	<3 (-13)	<2 (-12)	<2 (-13)	<1 (-13)	<1 (-13)
KK Oph	<5 (-13)	<9 (-13)	<4 (-13)	<4 (-13)	<3 (-13)
HD 158643	<1 (-12)	<2 (-12)	<1 (-12)	<1 (-12)	<8 (-13)
HD 163296	<2 (-12)	<2 (-11)	<2 (-12)	<2 (-12)	<2 (-12)
HD 169142	88 $\pm$ 7 (-14)	208 $\pm$ 1 (-13)	206 $\pm$ 6 (-14)	365 $\pm$ 6 (-14)	9 $\pm$ 5 (-14)
VV Ser	<3 (-13)	17 $\pm$ 2 (-13)	<3 (-13)	<2 (-13)	<2 (-13)
T CrA	<4 (-13)	<1 (-12)	<5 (-13)	<9 (-13)	<7 (-13)
HD 179218	<4 (-12)	<3 (-11)	<1 (-12)	<7 (-12)	<4 (-12)
WW Vul	<2 (-13)	<9 (-13)	<1 (-13)	<1 (-13)	<9 (-14)
HD 190073	<9 (-13)	<2 (-12)	<8 (-13)	<7 (-13)	<6 (-13)
LkHa 224	<6 (-13)	<7 (-13)	<3 (-13)	<5 (-13)	<3 (-13)
HD 203024	<5 (-13)	<9 (-13)	<4 (-13)	<2 (-12)	<3 (-13)

NOTE.—The line fluxes and errors are in  $\text{ergs cm}^{-2} \text{s}^{-1}$ , with  $a(b)$  representing  $a \times 10^b$ . For non-detections, the 3-sigma upper limit is given.

TABLE 5  
PAH-TO-STELLAR AND ALIPHATIC-TO-PAH LUMINOSITY RATIOS

Target	$L_{\text{PAH}}/L_{\star}$	$L_{\text{ali}}/L_{\text{PAH}}$
HD 31293	$44 \pm 2$ (-4)	$13 \pm 2$ (-3)
HD 31648	$25 \pm 5$ (-4)	$28 \pm 7$ (-3)
HD 34282	$1554 \pm 5$ (-5)	$7 \pm 1$ (-3)
HD 35187	$1228 \pm 9$ (-6)	$15 \pm 1$ (-3)
HD 36112	$13 \pm 2$ (-4)	$28 \pm 7$ (-3)
HD 244604	$13 \pm 3$ (-4)	$<2$ (-3)
HD 36917	$602 \pm 5$ (-6)	$5 \pm 2$ (-3)
BF Ori	$171 \pm 7$ (-6)	$<1$ (-2)
HD 37357	$9 \pm 1$ (-4)	$10 \pm 5$ (-3)
HD 37411	$34 \pm 1$ (-4)	$<1$ (-2)
RR Tau	$2097 \pm 8$ (-5)	$<2$ (-2)
HD 37806	$19 \pm 4$ (-4)	$21 \pm 5$ (-3)
HD 38120	$13 \pm 3$ (-4)	$3 \pm 1$ (-2)
HD 250550	$13 \pm 1$ (-4)	$34 \pm 9$ (-3)
V590 Mon	$328 \pm 2$ (-4)	$<1$ (-1)
HD 58647	$83 \pm 2$ (-6)	$<1$ (-1)
HD 72106S	$248 \pm 3$ (-5)	$5 \pm 2$ (-3)
HD 85567	$88 \pm 1$ (-5)	$11 \pm 2$ (-3)
HD 95881	$552 \pm 4$ (-5)	$6 \pm 2$ (-3)
HD 97048	$901 \pm 3$ (-5)	$6 \pm 2$ (-3)
HD 100453	$47 \pm 1$ (-4)	$8 \pm 1$ (-3)
HD 101412	$190 \pm 7$ (-5)	$11 \pm 5$ (-3)
HD 135344B	$180 \pm 2$ (-5)	$32 \pm 8$ (-3)
HD 139614	$254 \pm 4$ (-5)	$23 \pm 6$ (-3)
HD 141569	$353 \pm 2$ (-6)	$<1$ (-1)
HD 142666	$194 \pm 2$ (-5)	$28 \pm 2$ (-3)
HD 142527	$295 \pm 5$ (-5)	$36 \pm 2$ (-3)
HD 144432	$29 \pm 1$ (-5)	$21 \pm 4$ (-2)
HD 152404	$106 \pm 5$ (-6)	$<3$ (-2)
HD 169142	$605 \pm 2$ (-5)	$11 \pm 3$ (-3)
VV Ser	$411 \pm 6$ (-5)	$<1$ (-1)
WW Vul	$347 \pm 7$ (-6)	$<3$ (-2)

NOTE.—Only targets with a full 5–37- $\mu\text{m}$  IRS spectrum and with detected PAH emission are included.  $a$  ( $b$ ) represents  $a \times 10^b$ .

TABLE 6  
CORRELATIONS

Parameters			p-value
Cen 7.8 $\mu\text{m}$	$T_{\text{eff}}$	$\searrow$	$4 \times 10^{-3}$
PP 7.8 $\mu\text{m}$	$T_{\text{eff}}$	$\searrow$	$2 \times 10^{-3}$
FWHM 7.8 $\mu\text{m}$	$T_{\text{eff}}$	$\searrow$	$6 \times 10^{-3}$
Cen 6.2 $\mu\text{m}$	$T_{\text{eff}}$	$\searrow$	$4 \times 10^{-3}$
PP 6.2 $\mu\text{m}$	$T_{\text{eff}}$	$\searrow$	$5 \times 10^{-4}$
LF 8.6/6.2	$T_{\text{eff}}$	$\nearrow$	$2 \times 10^{-3}$
LF 8.6/7.8	$T_{\text{eff}}$	$\nearrow$	$5 \times 10^{-3}$
$L_{\text{ali}}/L_{\text{PAH}}$	$T_{\text{eff}}$	$\searrow$	$3 \times 10^{-2}$
LF 8.6/ali	$T_{\text{eff}}$	$\nearrow$	$3 \times 10^{-3}$
FWHM 7.8 $\mu\text{m}$	Cen 7.8 $\mu\text{m}$	$\nearrow$	$1 \times 10^{-3}$
LF 8.6/6.2	Cen 7.8 $\mu\text{m}$	$\searrow$	$1 \times 10^{-3}$
LF 8.6/7.8	Cen 7.8 $\mu\text{m}$	$\searrow$	$4 \times 10^{-4}$
$L_{\text{ali}}/L_{\text{PAH}}$	Cen 7.8 $\mu\text{m}$	$\nearrow$	$4 \times 10^{-3}$
LF 8.6/ali	Cen 7.8 $\mu\text{m}$	$\searrow$	$3 \times 10^{-3}$
LF 8.6/6.2	$L_{\text{ali}}/L_{\text{PAH}}$	$\searrow$	$1 \times 10^{-2}$
LF 8.6/7.8	$L_{\text{ali}}/L_{\text{PAH}}$	$\searrow$	$4 \times 10^{-3}$

NOTE.—A summary of the correlations indicating the dependence of the hydrocarbon chemistry upon the stellar radiation field. The arrows indicate a positive or negative correlation. The p-value is the probability of a non-correlation. Cen: centroid position; PP: peak position; LF: line flux ratio; FWHM: full width at half maximum; ali: the aliphatic 6.8 and 7.2- $\mu\text{m}$  CH features.